Effects of Y$_2$O$_3$ nanoparticles on the high-temperature oxidation behavior of IN738LC manufactured by laser powder bed fusion

Guo, Chuan; Yu, Zhengrong; Liu, Chang; Li, Xinggang; Zhu, Qiang; Ward, Mark

[Link to publication on Research at Birmingham portal](#)

Effects of Y_2O_3 nanoparticles on the high-temperature oxidation behavior of IN738LC manufactured by laser powder bed fusion

Chuan Guo[a,b,c], Zhengrong Yu[a,b], Chang Liu[b,d], Xinggang Li[b,e], Qiang Zhu[a,b*],

R. Mark Ward[c]**

[a] Department of Mechanical and Energy Engineering, Southern University of Science and Technology, Shenzhen 518055, PR China

[b] Shenzhen Key Laboratory for Additive Manufacturing of High-p]]

erformance Materials, Shenzhen 518055, PR China

[c] School of Metallurgy and Materials, University of Birmingham, Edgbaston, Birmingham B15 2TT, UK

[d] School of Innovation and Entrepreneurship, Southern University of Science and Technology, Shenzhen 518055, PR China

[e] Academy for Advanced Interdisciplinary Studies, Southern University of Science and Technology, Shenzhen 518055, PR China

*Corresponding author 1: Qiang Zhu

E-mail address: zhuq@sustech.edu.cn

**Corresponding author 2: R. Mark Ward

E-mail address: R.M.Ward@bham.ac.uk

Abstract: Oxidation tests at 1095 ^{o}C were performed on cubes of IN738LC doped with Y_2O_3 nanoparticles processed by laser powder bed fusion (LPBF). Adding Y_2O_3 nanoparticles led to grain

coarsening and the formation of $Y_4Al_2O_9$, both of which were expected to lead to reduced corrosion resistance in this alloy through a change from an Al-type oxide scale to Cr-type. However, 0.05 wt% Y_2O_3 addition was found to nonetheless be beneficial for corrosion resistance. Results and mechanisms for this were discussed and further work was recommended, in particular for the grain coarsening.

Keywords: Nickel-based superalloy, yttria, laser powder bed fusion, high-temperature oxidation

1. Introduction

Additive manufacturing (AM) is a novel manufacturing technology being used to fabricate or repair complex components in a layer by layer manner, which is nowadays attracting more and more attention from both engineering and research communities. Laser powder bed fusion is a type of powder bed AM technology with metallic powders as feedstock and has the ability to fabricate components with high precision [1]. In this process, powders with the size range from 15 μm to 53 μm are melted with a high-energy laser beam selectively under the control of a computer system [2]. After solidification, strong metallurgical bonds are formed between materials within a layer. Then the building substrate moves down by one-layer distance, and another layer is spread by a recoater [3]. This process is repeated until the whole component is completed.

The nickel-based superalloy Inconel 738LC (IN738LC) is mainly strengthened by fine γ′ precipitates with Ni_3(Al, Ti) chemical composition and $L1_2$ crystallographic structure [4] and is now being explored for use in LPBF. IN738LC has been widely used in the aerospace industry, such as for turbine blades, vanes and heat shields, etc. [5], which require high strength and excellent oxidation resistance at elevated temperatures. Recently, IN738LC has been applied to manufacture components using LPBF in order to achieve the challenging requirements of producing complex shapes with excellent properties [6-8].

The flexibility of LPBF provides an opportunity for making high-quality composites by directly introducing external particles to original powders using a mixture of powder or ball milling process [9,10]. Xia et al. [11] mixed 20 wt% WC ceramic particles into Inconel 718 powders and built parts by LPBF. They found that the micro-hardness and the ultimate tensile strength were enhanced due to the refined Ni_2W_4C particles between the primary dendrites and the fine (Nb, M)C particles in the matrix. Martin et al. [12] decorated TiB_2 nanoparticles onto Al7075 powders and successfully fabricated high-strength aluminum alloys using LPBF. And the performance of the material could be comparable to that of the wrought alloy. Song et al. [13] showed that the strength of the alloy manufactured by LPBF from Fe powders with ball-milled 2.2 wt% SiC particles was significantly improved. Compared with pure iron, Fe/SiC samples displayed a higher ultimate tensile strength that could reach 764 MPa due to the fine-grain and particulate strengthening mechanisms. In particular, oxide dispersion strengthened (ODS) alloys can be produced when some oxide particles (ThO_2, Y_2O_3, Al_2O_3, etc.) are added into the material matrix [14] and improved physical and mechanical properties can be obtained [15]. Li et al. [16] found that the addition of La_2O_3 was helpful to fabricate a crack-free coating in the laser cladding process and also led to high micro-hardness and good corrosion resistance. Sun et al. [14] investigated the effect of Y_2O_3 additions on the high-temperature oxidation behavior of ODS Ni-20Cr-5Al alloy and found that the alloy with the addition of 0.2 wt% Y_2O_3 showed the best oxidation resistance. Chen et al. [17] examined the oxidation behavior of 9 at% Cr ODS ferritic/martensitic steel exposed to supercritical water at different application temperatures. They suggested that the oxidation resistance was improved from a small quantity of yttrium (0.28 wt%) because the element migration was accelerated in the microstructure, which was beneficial for the formation of a continuous spinel layer.

However, there is as yet little information on the microstructural characteristics, tensile strength and oxidation resistance of IN738LC manufactured by the LPBF process with the addition of Y_2O_3 nanoparticles. In the present study, the oxidation behavior at 1095 ºC of IN738LC doped with nano-sized Y_2O_3 particles processed by LPBF was investigated. The structure of the oxide scales and the oxidation products were systematically analyzed. The oxidation mechanisms and the effects of Y_2O_3 were also discussed.

2. Experimental procedure

2.1 Material preparation

Argon-atomized IN738LC powders produced by the AMC POWDER Co., Ltd were used in this study. The powders had a size distribution of D_{10} = 18.9 µm, D_{50} = 30.1 µm and D_{90} = 47.4 µm. The Y_2O_3 particles were from Shanghai Shuitian material technology Co., Ltd with an average size of 100 nm. The chemical composition of the IN738LC powder is given in Table 1. Morphologies of the IN738LC and Y_2O_3 powders were observed by a ZEISS Merlin scanning electron microscope (SEM), as shown in Fig. 1a and Fig. 1b, respectively. The nano-sized Y_2O_3 particles were introduced into the IN738LC powders with the content of 0 wt%, 0.05 wt%, 0.2 wt% and 0.6 wt% using a Turbula T2F 3D swing mixer for 3 h. Fig. 1c-f shows the composites of the Y_2O_3 nanoparticles and the IN738LC powders and the insert images exhibit the details of the powder surfaces in high magnification.

Ni	Co	Cr	W	Ta	Ti	Al	Mo	Nb	Zr	B	C
Bal.	8.47	15.83	2.67	1.63	3.41	3.36	1.71	0.74	0.06	0.009	0.1

Table 1 Chemical composition of the IN738LC powder in wt%.

2.2 LPBF process

An SLM solutions 125 system equipped with a continuous wave IPG fiber laser with a maximum

output of 400 W and maximum scan speed 10 m/s was used to manufacture the test samples with dimensions of 50 mm × 15 mm × 10 mm. A 67° raster scan strategy was used, in which the scanning directions were uniform in a layer and rotated 67° between layers. Other processing parameters in this study are listed in Table 2.

Laser power	Scan speed	Hatch distance	Layer thickness	Preheated
270 W	950 mm/s	90 μm	30 μm	200 °C

Table 2 Parameters used in the LPBF process.

2.3 High-temperature oxidation tests

A standard heat-treatment was carried out before the oxidation tests. It consisted of a solution treatment at 1120 °C for 2 h followed by air cooling and then an aging treatment at 850 °C for 24 h followed by air cooling [18]. Afterwards, all the samples were sectioned into dimensions of 15 mm × 10 mm × 5 mm (with the surface with the size of 15 mm × 10 mm parallel to the building direction), polished down to 3000 CW and ultrasonically cleaned in ethanol for 5 min. Al_2O_3 crucibles were used to hold the samples for the oxidation tests. In order to eliminate the effects of moisture in the holders, the Al_2O_3 crucibles were preheated to 1000 °C for 24 h and cooled down to room temperature. All the preheated Al_2O_3 crucibles were weighed. The preheating process was repeated until the weight of these crucibles kept constant. Then the Al_2O_3 crucibles, together with the samples, were exposed at 1095 °C in an air atmosphere for 240 h altogether in a high-temperature furnace (KSL-1200X). The furnace has a 5 mm hole connecting to the outside air in order to guarantee enough oxygen to react with the samples. After every 24 h, all the samples were taken out from the furnace, cooled down to room temperature and measured for total mass together with the crucibles. The oxidation behavior was investigated by the mass gain per unit area of the samples over the heated time. There were three samples for each

alloy and the results were the average values.

2.4 Material characterization

Microstructural observation after the standard heat treatment was carried out by an EDAS Digiview 4 Electron backscattered diffraction (EBSD) and a Talos F200X transmission electron microscope (TEM) with an energy dispersive spectrometry (EDS) under 200 kV before the oxidation tests. The thin foils for TEM were prepared using an electrolytic twin-jet thinning system (Struers TenuPol-5) in a solution of 10% perchloric acid ethanol under 15 V for 5 min below -15 °C. EBSD was conducted on the largest surface (the surface with the size of 15 mm × 10 mm) parallel to the building direction in order to investigate the grain size distribution of the samples. The average grain size was obtained by scanning nine different view-fields for each sample with the software TSL OIM Analysis 7 64×. The samples for EBSD were prepared by a Buehler VibroMet 2 vibratory polisher in OPS suspension for 3 h. The oxide scale surfaces were observed with a KEYENCE laser scan confocal microscope (LSCM) and a ZEISS Merlin SEM with an EDAX Octane Pro EDS under 15 kV. Cross-sections of the oxide scales were ground sequentially by 240 CW, 600 CW, 1000 CW, 1500 CW, 2000 CW and then polished down to 0.04 colloidal silica suspension for the SEM observation and the EDS test. ECO X-ray diffraction (XRD) testing was conducted with a Cu-K$^{\alpha}$ source and a ceramic X-ray tube at 40 kV and 25 mA on the oxide scale surfaces from 20º to 80º. The relative density of the samples was obtained by the image threshold technique with Image J, i.e., using the characteristics of color differences between materials and defects such as pores, cracks, etc., on the polished surfaces. Seven images were taken into consideration for each alloy composition, and the quoted results were the averaged values.

3. Results

3.1 Microstructure before oxidation

Fig. 2 shows the TEM image of the alloy containing 0.05 wt% Y_2O_3, revealing the distribution of the added nano-sized particles. These particles were found scattered in the material with a size range between 20 nm and 50 nm. In addition, the bimodal distribution of the primary and secondary γ' phases was visible. The average sizes of the cuboidal primary γ' and fine secondary γ' precipitations were about 350 nm and 50 nm, respectively. Fig. 3 is an EDS mapping image of the nano-sized particle. The enrichment of Al, Y and O is apparently shown in the EDS results, which supports the identification of these particles as being of the Y–Al–O type. Fig. 4a shows an example of the particle in high magnification. The corresponding Fast Fourier Transformation (FFT) image of the nano-sized particle is presented in Fig. 4b. This result is in good agreement with the monoclinic crystal structure YAM phase, i.e., $Y_4Al_2O_9$ with zone axis of [1 -1 0]. The inverse pole figures (IPFs) with respect to the building direction by EBSD of the LPBF-processed IN738LC components under the conditions for adding various amounts of Y_2O_3 are depicted in Fig. 5. It is apparent that the grain size continued increasing with the addition of Y_2O_3. The average grain size increased from 57.4 μm to 72.1 μm when 0.05 wt% Y_2O_3 was added. Subsequently, the average sizes of the alloys containing 0.2 wt% Y_2O_3 and 0.6 wt% Y_2O_3 were 81.9 μm and 103.4 μm, respectively.

3.2 Oxidation kinetics

Fig. 6a shows the mass gain of the LPBF-processed IN738LC components under the conditions for adding various amounts of Y_2O_3 as a function of the exposure time at 1095 ºC in the air atmosphere. It is evident that the mass gain increased continuously with the time for all the samples. The alloy containing 0.6 wt% Y_2O_3 exhibited the highest oxidation rate among these alloys, followed by the alloy containing 0.2 wt% Y_2O_3 and the alloy without Y_2O_3. The alloy containing 0.05 wt% Y_2O_3 had

the best oxidation resistance. Fig. 6b shows the mass gain rate as a function of the exposure time. The mass gain rate was calculated as:

$$r_i = \frac{(\Delta m / A)_i - (\Delta m / A)_{i-1}}{T} \tag{1}$$

where r_i is the mass gain rate in the current testing period, Δm is the mass change, A is the surface area, $(\Delta m / A)_i$ is the mass change per unit area in the current testing period, $(\Delta m / A)_{i-1}$ is the mass change per unit area in the previous testing period and T is the testing period, i.e., 24 h. For all the samples, the mass gain rate generally showed a gradual downward trend with the exposure time, implying that the oxidation rate gradually slowed down with the progress of the oxidation tests. The oxidation kinetics curve in Fig. 6a can be described as a parabolic shape like [19]:

$$(\frac{\Delta m}{A})^2 = k_p t \tag{2}$$

where k_p is the parabolic oxidation rate constant, t is the time. The lower the k_p value is, the better the oxidation resistance. The summary of the fitting results is listed in Table 3 and all the coefficients of determination R^2 were close to 1, indicating that the results fit well with a parabolic curve as described in Eq. (2). It can be seen that the addition of 0.05 wt% Y_2O_3 improved the oxidation resistance significantly. Compared with the alloy without Y_2O_3, the oxidation rate constant k_p decreased from 0.56 $mg^2cm^{-4}h^{-1}$ to 0.39 $mg^2cm^{-4}h^{-1}$. However, with the further increase of Y_2O_3 content, the oxidation resistance decreased and the k_p values increased to 0.73 $mg^2cm^{-4}h^{-1}$ and 1.17 $mg^2cm^{-4}h^{-1}$ for the alloys containing 0.2 wt% and 0.6 wt% Y_2O_3, respectively.

Y_2O_3 content (wt%)	0	0.05	0.2	0.6
k_p ($mg^2cm^{-4}h^{-1}$)	0.56	0.39	0.73	1.17
R^2	0.94	0.94	0.96	0.97

Table 3 Oxidation rate constant k_p in Eq. (2) by fitting the experimental results.

3.3 Oxide scale surface

Fig. 7 shows the surface roughness (Ra) and the 3D reconstruction images of the oxide scale surfaces by LSCM of the LPBF-processed IN738LC components with varying amounts of Y_2O_3 after the oxidation test at 1095 °C for 240 h. The alloy without Y_2O_3 had a surface roughness of 7.6 μm and a small nodular morphology was visible on the oxide scale surface (Fig. 7a). For the alloy containing 0.05 wt% Y_2O_3, a relatively flat surface was attained and the surface roughness decreased to 5.5 μm. With increasing Y_2O_3 content, the oxide scale surfaces became rougher and more irregular with a surface roughness of 11.1 μm for the alloy containing 0.2 wt% Y_2O_3 and 13.7 μm for the alloy containing 0.6 wt% Y_2O_3. Large nodular structures appeared on these oxide scale surfaces, as shown in Fig. 7c and d, accordingly leading to a higher surface roughness. For all the alloys, spalled zones were detectable on the oxide scale surfaces, which also reduced the surface quality. From the surface reconstruction images, it seems that the spallation phenomenon was more severe for the alloys containing 0.2 wt% and 0.6 wt% Y_2O_3.

Fig. 8 illustrates the oxide scale surface morphologies by SEM of the alloy samples in both low and high magnifications after the oxidation tests at 1095 °C for 240 h. It is apparent that the morphology of the oxide scale surfaces of IN738LC fabricated by LPBF was affected by the addition of Y_2O_3. A reasonably flat oxide scale was observed on the surfaces of the alloy without Y_2O_3 (Fig. 8a) and the alloy with 0.05 wt% Y_2O_3 (Fig. 8c). While the additions of 0.2 wt% and 0.6 wt% Y_2O_3 led to a large number of nodular structures on the oxide scale surfaces, as shown in Fig. 8e-h.

3.4 Oxidation product

Fig. 9 shows the XRD analysis results of the LPBF-processed IN738LC components with varying

amounts of Y_2O_3 after the oxidation tests at 1095 ℃ for 240 h. It shows that the main oxidation products were Al_2O_3, Cr_2O_3, NiO, $NiCr_2O_4$ and $CoCr_2O_4$. From the signal intensity in the XRD results, it shows that a large amount of Al_2O_3 was formed in the oxide scale for the alloy without Y_2O_3. With increasing Y_2O_3 content, the diffraction peaks of Cr-rich oxides became stronger and $NiCr_2O_4$, $CoCr_2O_4$ and Cr_2O_3 were considered as the primary oxidation products in the alloys containing 0.2 wt% and 0.6 wt% Y_2O_3. On the contrary, the intensity level of Al_2O_3 was lower than that for the alloy without Y_2O_3.

Three different morphologies were observed on the oxide scale surfaces, namely crystalline, lamellar and nodular structures, as presented in Fig. 10. The crystalline structure contained Cr, O, Ni, Ti and Co, as shown in Fig. 10g, which is considered to be a type of Cr-rich oxide. This kind of oxide was observed in all the samples among the four alloys. Fig. 10h shows that the lamellar oxide mainly contained Al and O. Combined with the results of XRD, it indicates the presence of Al_2O_3. Al_2O_3 was visible in the alloy without Y_2O_3 and the alloy containing 0.05 wt% Y_2O_3 but only rarely in the alloys containing 0.2 wt% and 0.6 wt% Y_2O_3. EDS detected a large amount of Ni and O, implying that the nodular structure primarily consisted of NiO, as shown in Fig. 10i. These nodular structures scattered on the oxide scale surfaces were commonly observed in the alloy without Y_2O_3 and the alloys containing 0.2 wt% and 0.6 wt% Y_2O_3. Detailed observation, however, showed that NiO also existed in the alloy containing 0.05 wt% Y_2O_3 as a blocky morphology (black arrow) ranging from 0.5 μm to 5 μm, as shown in Fig. 11a and Fig. 11b is the EDS result.

Fig. 12 shows the EDS chemical mapping analysis results of the oxide scale for the LPBF-processed IN738LC component without Y_2O_3 after the oxidation tests at 1095 ℃ for 240 h. It can be seen that the oxidation products were mainly composed of O, Al and Cr, but heterogeneously

distributed in the oxide scale. The Al_2O_3 and Cr-rich oxides were found to compete with each other, i.e., little Cr-rich oxide was found in regions rich in Al_2O_3 and vice versa. Because Al_2O_3 was the main constituent that occupied a large part of the oxide scale, therefore, this scale is defined as an Al-type scale. The enrichment of Cr was observed to be associated with O in the oxide scale, which is therefore considered as Cr-rich oxide. It is worth noting that a thin layer rich in Cr can be seen in the outer layer of the oxide scale. Combined with the XRD results, it is reasonable for this layer to be considered as spinel oxides such as $CoCr_2O_4$ and $NiCr_2O_4$. However, the microstructure and the chemical composition distribution were found to be quite different for the alloy containing 0.6 wt% Y_2O_3, as shown in Fig. 13. It is apparent that this scale was instead composed largely of oxides with a high concentration of Cr. In this Cr-type oxide scale, however, the formation of Al_2O_3 was only found underneath the Cr-rich layer, with an irregular and discontinuous morphology extending down into the parent metal.

Fig. 14 shows the SEM cross-sections of the oxide scales of the LPBF-processed IN738LC components for the alloy without Y_2O_3 and the alloy containing 0.05 wt% Y_2O_3 in both low and high magnifications after the oxidation tests at 1095 ºC for 240 h. Similar to Fig. 12, it can be seen that the oxide scale consisted of a thin upper Cr-rich layer (5-10 μm typically) and a thicker Al_2O_3 sublayer (15-25 μm typically). The compositions are shown in Fig. 14e and f from EDS analysis. Both of these layers were mostly continuous. The parent metal beneath these layers was fully continuous. By contrast, in Fig. 15, for the alloys containing 0.2 wt% and 0.6 wt% Y_2O_3, the parent metal beneath the oxide scales can be seen to have been strongly discontinuous, with significant jagged lines of Al_2O_3 presence (Fig. 15e). But now there was no longer a mostly-continuous Al_2O_3 layer near the surface, just a Cr-rich layer (Fig. 15f). These observations are consistent with the higher-magnification results shown in

Fig. 13.

4. Discussion

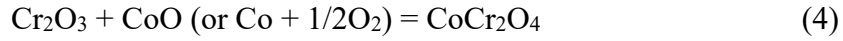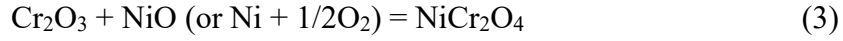### 4.1 Effects of Y_2O_3 on the microstructure before oxidation

Fig. 5 indicates that the addition of Y_2O_3 led to the coarsening of the grains in the microstructure. Some particles are known to be heterogeneous nucleation centers, which can effectively refine the grains in materials [20,21]. In the present investigation, however, the grains were coarsened to nearly double their original size with the addition of 0.6 wt% Y_2O_3 rather than being refined. Wilms et al. [22] suggested that there was a poor wettability of Y_2O_3 by the Ni-Cr melt in stainless steel manufactured by the laser AM process, where grain refinement by Y_2O_3 was not observed. In the IN738LC parts produced in this work, it could be argued that this is due to a reduction in thermal diffusivity during solidification because $Y_4Al_2O_9$ can be used as a type of thermal barrier material due to its low high-temperature thermal conductivity [23]. The thermal conductivity of $Y_4Al_2O_9$ is about 1.56 W/m/K at 1273 K [24], which is much lower than that of IN738LC (24.9 W/m/K) [25]. Therefore, a sufficient amount of dispersed nano-sized $Y_4Al_2O_9$ particles could retard the heat dissipation from the current location to the surrounding materials in the process of solidification, thus decreasing the cooling and solidification rate of the melt and leading to the formation of coarser grains. However, the amount of Y_2O_3 was added at a very low level. There are, therefore, significant doubts that these particles could have so strong an effect on the thermal properties as to be the route to influence the microstructure. Instead, the authors propose that this should be an area of future investigation.

The effects of grain size on the oxidation behavior have been widely investigated among metallic and ceramic materials [26,27]. Jo et al. [28] examined the internal oxidation behavior of as-received and grain-refined Alloy 617 at 950 °C up to 2000 h. They found that the internal oxidation rate of the

grain-refined alloy increased rapidly in the initial stage of the tests and gradually decreased during prolonged exposure, while the as-received alloy exhibited a constant oxidation rate during the whole oxidation process. Besides, large cracks were observed due to the high stress concentration from the longer internal oxides in the as-received alloy. By contrast, short cracks in the grain-refined sample were scattered near the surface due to the relatively low stress concentration related to more densely stretched internal oxides. Pérez [29] suggested that fine grains were beneficial for oxidation resistance due to increased nucleation of Al_2O_3 particles, which led to the formation of a pure Al_2O_3 scale and accordingly increased the oxidation resistance. Generally, the improvement of oxidation resistance by refined grains is widely reported [30,31], which is primarily due to the acceleration of diffusion of some protective elements to form oxide scales related to more grain boundaries. In the present study, the addition of Y_2O_3 led to coarse grains, which probably was the cause of the increased oxidation rate, as shown in Fig. 6. However, 0.05 wt% Y_2O_3 was favorable to improve the oxidation resistance. Therefore, the oxidation mechanisms and the effects of Y_2O_3 need to be further investigated.

4.2 Effects of Y_2O_3 on the oxidation behavior

Based on the results of EDS and XRD, the main oxidation products found in these experiments were Al_2O_3, Cr_2O_3, NiO, $NiCr_2O_4$ and $CoCr_2O_4$. According to oxidation kinetics, the more stable the oxide is, the more preferentially the corresponding element is oxidized. In the alloy systems of Ni-Cr-Al such as IN738LC, oxidation priority of the main elements is Al > Cr > Ni, indicating Al_2O_3 is formed firstly followed by Cr and Ni oxides. However, the affinity with O_2 is not the only factor deciding the oxidation behavior [14]. The formation of Al_2O_3 has an important effect of hindering O_2 diffusion, thus preventing the oxidation progress with other elements in the parent alloy. Cr_2O_3 can react with NiO and CoO to form $NiCr_2O_4$ and $CoCr_2O_4$ by the reactions:

$$Cr_2O_3 + NiO \text{ (or } Ni + 1/2O_2) = NiCr_2O_4 \tag{3}$$

$$Cr_2O_3 + CoO \text{ (or } Co + 1/2O_2) = CoCr_2O_4 \tag{4}$$

XRD also indicated the formation of $NiCr_2O_4$ and $CoCr_2O_4$, as shown in Fig. 9. $NiCr_2O_4$ and $CoCr_2O_4$ belong to the group of spinel oxide [14,32] and its typical morphology is shown in Fig. 10a and d. Zhou et al. [33] proposed that Ni cations diffused slowly in the structure of $NiCr_2O_4$, indicating that $NiCr_2O_4$ could inhibit the diffusion of Ni cations and thus improve the oxidation resistance. Sun et al. [14] believed that $NiCr_2O_4$ improved the compactness of the oxide scale and further prevented the alloy from reacting with O_2.

YCrO$_3$ was found in some previous studies [14] of the alloy containing Y_2O_3 during the oxidation tests. YCrO$_3$ is formed according to the reaction:

$$Cr_2O_3 + Y_2O_3 = 2YCrO_3 \tag{5}$$

YCrO$_3$ is a type of perovskite structure with symmetric P*bnm* space. The melting point of YCrO$_3$ is about 2290 °C [34]. The high thermal and structural stabilities lead it to be considered as inclusions in the oxide scale, which deteriorate the exfoliation resistance. Moreover, Sun et al. [14] reported that YCrO$_3$ favored creating compressive stress on crystal grains of the matrix phase and then the oxide scale tended to crack and peel off with the accumulation of stress. However, the YCrO$_3$ peak was not found in the XRD analysis in this study since it is difficult to produce a complete diffraction pattern for XRD to detect when the content of a phase is too low in the multiphase mixture.

From Fig. 6, adding 0.05 wt% Y_2O_3 reduced the oxidation rate of the LPBF-processed IN738LC component. The result is consistent with some previous reports for Fe-Cr alloy [35] and austenitic stainless steel [36]. In the study of Stringer et al. [37], rare earth element oxide particles such as Y_2O_3, CeO_2, etc., can act as nucleation centers for oxides, especially Cr_2O_3, thereby promoting the formation

of Cr_2O_3. It is possible that more spinel oxides, i.e., $NiCr_2O_4$ and $CoCr_2O_4$, were formed in the oxidation cycle in the alloy containing 0.05 wt% Y_2O_3, related to the observation in Fig. 14 and the XRD analysis in Fig. 9. As a result, the oxidation rate was reduced due to the presence of spinel oxides. Moreover, Bautista et al. [38] believed that Y_2O_3 improved the adherence and the resistance to spallation of the oxide scale, which was also favorable to improve the oxidation resistance of alloys. However, it was found that the further increase of Y_2O_3 up to 0.2 wt% had a negative effect on the oxidation resistance. This is ascribed to the low amount of Al_2O_3 in the oxide scales of the alloys containing 0.2 wt% and 0.6 wt% Y_2O_3, as Al_2O_3 is believed to be more effective to prevent materials from being oxidized than Cr_2O_3 [39].

Generally, the oxides were mainly composed of Al_2O_3 for the alloy without Y_2O_3 and the alloy containing 0.05 wt% Y_2O_3, as depicted in Fig. 14. While when more nano-sized Y_2O_3 particles were added to the IN738LC alloy, Cr_2O_3 and other Cr-rich oxides became the dominant oxides in the scale and the formation of Al_2O_3 was largely limited to jagged regions penetrating down into the parent metal. The change of the oxide scale from Al-type to Cr-type by the addition of Y_2O_3 in the LPBF-processed IN738LC components can be explained by the finding of Giggins et al. [40] in 1971. They argued that there were three different mechanisms of oxidation in the system of Ni-Cr-Al according to the different composition of the alloy. The oxide scale in the first mechanism (I) consists of a layer of NiO with a subscale of Al_2O_3 and Cr_2O_3 in the matrix, while the second (II) type is a layer of Cr_2O_3 with an Al_2O_3 subscale in the matrix and the third (III) one is a continuous layer of Al_2O_3. Fig. 16 presents the isothermal diagram exhibiting the compositional limits for these three mechanisms of oxidation in the Ni-Cr-Al system. The chemical composition of IN738LC is almost at the borderline between Mechanism II and Mechanism III, indicating even a slight reduction in Al content can

completely change the oxidation behavior of the IN738LC alloy. It is worth noting that the added Y_2O_3 could react with Al to form $Y_4Al_2O_9$, which effectively consumed Al in the composition of the alloy, as shown in Fig. 3. Presumably, the addition of Y_2O_3 reduced the amount of Al, inducing the change of the oxide scale from a continuous layer of Al_2O_3 (Mechanism III, Fig. 14) to a layer of Cr_2O_3 with an Al_2O_3 subscale in the parent alloy (Mechanism II, Fig. 15).

Furthermore, Lou et al. [41] suggested that the increase of grain size altered the oxide scale formed on the surface from Al-type into Cr-type, where the diffusion of Al atoms was delayed due to the relatively small number of grain boundaries in the coarse microstructure. The minimum Al concentration N_{Al} required to form an Al_2O_3 scale in the pure oxidizing condition is given by Wagner [42,43]:

$$N_{Al} = (\frac{\pi g V_m N_o D_o}{3V_{ox}D_{Al}})^{0.5} \tag{6}$$

where g is a constant near 0.3, V_m is the molar volume of the alloy, N_o is the concentration of O atoms, D_o is the diffusivity of O atoms in the alloy, V_{ox} is the molar volume of Al_2O_3 and D_{Al} is the diffusivity of Al atoms in the alloy. It is well believed that the diffusion at grain boundaries is much more rapid than that inside the grains. The addition of Y_2O_3 led to coarse grains and a relatively small number of grain boundaries, which decreased the diffusivity of Al atoms and further increased N_{Al}. Therefore, the critical Al concentration required for the formation of the Al_2O_3 scale was increased, indicating that the Al_2O_3 scale was suppressed. On the contrary, the formation of Al_2O_3 was facilitated by the relatively fine microstructure in the alloy without Y_2O_3.

4.3 Oxidation scale spallation

From Fig. 7 and Fig. 8, the high surface roughness was primarily attributed to the spallation phenomenon and the nodule structures on the oxide scale surfaces. Spallation occurs when the stress

is larger than the adhesion between the parent alloy and the oxide scale in materials [44]. Severe

spallation of the oxide scales for the alloys containing 0.2 wt% and 0.6 wt% Y_2O_3 after the oxidation

tests at 1095 °C for 240 h can be found in Fig. 17a-d. It was seen that the oxide scales cracked and

tended to peel off from the parent alloy, which played an important role resulting in a high oxidation

rate.

Fig. 18 shows the relative density as a function of the Y_2O_3 content. It can be seen that the relative

density for the alloy without Y_2O_3 was similar to that for the alloy containing 0.05 wt% Y_2O_3, i.e.,

99.66% and 99.43%, respectively. While when the contents of Y_2O_3 increased to 0.2 wt% and 0.6 wt%,

the relative densities decreased to 99.06% and 98.85%, respectively. Sun et al. [14] suggested that

defects were generated due to the development of a weak nanoparticle-matrix bonding when excess

nanoparticles were added related to the grain boundary segregation and the capillary force. Evans et

al. [45] reported that the oxide scale wrapped first at the "pre-existing interfacial flaw" under the action

of compressive stress or tensile stress perpendicular to the interface generated on the periphery of

warping, leading to the expansion of warping and cracks in the oxide scale. Spallation will occur when

the cracks go through the oxide scale. Similarly, Rahmel et al. [46] summarized the critical strain

equation for the oxide scale rupture:

$$-\varepsilon_c = \frac{K_{IC}}{f(\pi a)^{1/2}} \cdot \frac{1+r/d}{2E_O/(1+\upsilon_O)} \qquad (7)$$

where $-\varepsilon_c$ is the critical strain, K_{IC} is the fracture toughness, f is the geometric factor, a is the size of

defect at the interface, r is the length of oxide intrusion into the matrix for a wavy interface, d is the

thickness of oxide scale, E_O is the elasticity modulus of oxide scale, and υ_O is the Poisson's ratio of

oxide scale. According to Eq. (7), the large defects and the thick oxide scales in the alloys containing

0.2 wt% and 0.6 wt% Y_2O_3 were favorable to reduce the value of $-\varepsilon_c$ and directly increased the risk of

spallation.

The Pilling-Bedworth ratio (PBR) [47] is defined as the ratio of oxide volume to metal volume and can be determined in Eq. (8):

$$PBR = \frac{M_O \times \rho_M}{A_M \times i \times \rho_O}$$ (8)

where M_O is the molar mass of oxide molecules, ρ_M is the density of metal, A_M is the molar mass of metal atoms, ρ_O is the density of oxide and i is the number of metal atoms in the corresponding oxide molecule. PBR is useful to determine the integrity of an oxide scale. The higher the PBR value is, the more easily the oxide scale peel off. The values used to calculate PBRs can be found in Table 4 [48]. Using Eq. (8), the calculated PBRs of Al_2O_3, NiO and Cr_2O_3 are 1.29, 1.68 and 2.01, respectively, indicating that Cr_2O_3 is more likely to peel off due to its high internal stress during the repeated heating and cooling process in the oxidation cycle. The stress related to PBR in the oxidation process can be determined as [49,50]:

$$\sigma_{PBR} = \frac{E_o}{1-\upsilon_o}(1-(PBR)^{1/3})$$ (9)

where E_o is the Young's modulus of the oxide, υ_o is the Poisson's ratio of the oxide. And the σ_{PBR} for Al_2O_3 and Cr_2O_3 are 42.02 GPa and 102.19 GPa (the relative values used in the calculation are listed in Table 4), respectively, implying the stress generated in Cr_2O_3 scale is much larger than that in Al_2O_3 scale.

	M_O (mol/g)	ρ_M (g/cm³)	A_M (mol/g)	i	ρ_O (g/cm³)	E_o (GPa)	υ_o	α_o ($\times 10^{-6}$ /K)
Al_2O_3	101.96	2.7	26.98	2	3.96	370	0.22	9.6
NiO	74.69	8.88	58.69	1	6.72	N/A	N/A	N/A
Cr_2O_3	151.99	7.19	52	2	5.22	273	0.3	5.7

Table 4 Values used to calculate PBR, σ_{PBR} and σ_{CTE} [48,51].

Furthermore, cracking also results from the large difference in thermal expansion coefficients (CTEs) between oxide scales and alloys [51]. The corresponding stress in the oxide scale can be calculated by the following equation [52]:

$$\sigma_{CTE} = \frac{E_o}{1-\nu_o}(\alpha_o - \alpha_s)\Delta T \qquad (10)$$

where α is the thermal expansion coefficient, the subscripts s and o refer to the substrate and the oxide and ΔT is the temperature difference between the oxidation temperature and room temperature (1095 °C – 25 °C = 1070 °C). The thermal expansion coefficients of the parent alloy and the oxides can be found in Ref. [53] and Table 4, respectively. Using Eq. (10), the σ_{CTE} values are 3.2 GPa and 4.26 GPa for Al_2O_3 and Cr_2O_3, respectively. It is worth noting that although the σ_{CTE} of Cr_2O_3 is larger than that of Al_2O_3, the difference is very small compared to that in σ_{PBR}. In addition, σ_{PBR} is noticeably larger than σ_{CTE}. Actually, there are two assumptions about using PBR to estimate the stress generated in oxide scales during the oxidation process. First, all new oxides are formed within or beneath the scale (since there is no stress on free surfaces if these oxides are formed at the external). Moreover, the stress relief mechanism is also ignored. In this case, the stress calculated by Eq. (9) is the maximum possible value. Therefore, the σ_{PBR} is unrealistically large in this investigation.

In conclusion, the spallation tended to occur in the Cr-type scale, i.e., the alloys containing 0.2 wt% and 0.6 wt% Y_2O_3 due to the relatively large stress in the oxide scale, thus increasing the oxidation rate. From Fig. 17e, the EDS result in Region 2 proves that the spallation layer is Cr-rich. And peaks of Ta, Nb, etc., can be observed in Region 1 beside the spallation layer, indicating that the parent alloy was exposed to air due to the spallation.

4.4 Oxidation process

The effect of rare earth elements and/or their oxides on the oxidation behavior was widely reported in Al_2O_3-forming and Cr_2O_3-forming alloys and termed the "reactive element effect" (REE) [54]. It is based on two effects from reactive elements on the oxidation behavior, i.e., the ability to change the structure of oxide scales by affecting the oxidation mechanism and the ability to improve the adhesion of oxide scales [55]. Hou et al. [54] suggested that the reactive elements and their oxides could promote the formation of Cr_2O_3 scales on alloys by developing Cr_2O_3 scales with less Cr in the chemical composition and suppressing further oxidation process of the base metal in the presence of a stable Cr_2O_3 scale, which was related to the enhancement of Cr diffusion in the microstructure and oxide nucleation theory [37]. For the improvement of scale adhesion, three mechanisms [54] were proposed as (I) reducing the internal stress by modifying the scale growth mechanism, (II) enhancing the bonds at the alloy-scale interfaces and (III) increasing the toughness of existing scale, thus improving the exfoliation resistance of oxide scales.

In the present investigation, in which the addition of Y_2O_3 nanoparticles led to increased grain size in IN738LC components manufactured by LPBF, the following analysis is proposed. According to the formation mechanism of multilayer oxides in previous studies [56], a schematic diagram of the scale formation process of the LPBF-processed IN738LC components with various amounts of Y_2O_3 is proposed in Fig. 19. In the first stage, O_2 was adsorbed onto the surface of the alloy. Cr cations initially diffused towards the metal/oxide interface and firstly reacted with O_2. Cr_2O_3 nucleated on the surface as the outer oxide and more Cr_2O_3 was formed in Cr-type oxide scales when 0.2 wt% and 0.6 wt% Y_2O_3 were added. Subsequently, Ni cations migrated to the continuous Cr_2O_3 film and participated in the reaction between O_2 and Cr_2O_3 to form spinel $NiCr_2O_4$. Simultaneously, the oxidation reaction of Ni took place when the parent alloy was exposed to O_2 due to the spallation of

Cr_2O_3 and/or $NiCr_2O_4$ and the nodular NiO accordingly grew to the top surface of the oxide scale, as depicted in Step 2. In the Al-type scale, a large number of Al cations diffused towards the top surface, inducing Al_2O_3 to nearly occupy the whole sublayer (in the alloy without Y_2O_3 and the alloy containing 0.05 wt% Y_2O_3). However, the formation of Al_2O_3 was suppressed in the alloys containing 0.2 wt% and 0.6 wt% Y_2O_3, which might be primarily attributed to the thick Cr-rich layer hindering the reaction of O_2 and Al atoms [54]. Furthermore, the coarse grains in the Y_2O_3-containing alloys also inhibited the rapid formation of Al_2O_3 by slowing the diffusion of Al atoms due to the reduced grain boundaries in the microstructure, as discussed before.

5. Conclusion

1. It was found that the LPBF-processed IN738LC alloy grains were coarsened apparently with increasing Y_2O_3 content. It could be argued that this was due to the formation of the YAM phase, i.e., $Y_4Al_2O_9$, decreasing the cooling rate of the melt in the solidification process. However, the volume fraction of $Y_4Al_2O_9$ was thought to be much too low and this effect should, therefore, be investigated in future work.

2. Adding 0.05 wt% Y_2O_3 was found to improve the oxidation resistance, causing the oxidation rate constant k_p to decrease from 0.56 $mg^2cm^{-4}h^{-1}$ to 0.39 $mg^2cm^{-4}h^{-1}$. However, further additions to 0.2 wt% and 0.6 wt% Y_2O_3 increased the oxidation rate, and the k_p values were then 0.73 $mg^2cm^{-4}h^{-1}$ and 1.17 $mg^2cm^{-4}h^{-1}$, respectively.

3. The surface roughness of the oxide scale surface was 7.6 μm for the alloy without the addition of Y_2O_3, 5.5 μm for the alloy containing 0.05 wt%, 11.1 μm for the alloy containing 0.2 wt% and 13.7 μm for the alloy containing 0.6 wt% Y_2O_3. The main factors that affected the surface roughness of the oxide scale surfaces were the nodular structures and spallation.

4. The main oxidation products were Al_2O_3, Cr_2O_3, NiO, $NiCr_2O_4$ and $CoCr_2O_4$. The addition of sufficient Y_2O_3 was found to cause the oxide scale to become dominated by Cr-rich oxides, pushing the Al_2O_3 sublayer found in the oxide scale into jagged regions in the parent alloy.

5. The oxidation resistance of the LPBFed IN738LC components was found to be affected by many factors such as the characteristics of the oxide scale, the chemical composition of the alloy and the microstructure (grain size and defects), etc.

Acknowledgment

Reference

[1] Liu, Yang, Jian Zhang, Zhicong Pang, Weihui Wu, Investigation into the influence of laser energy input on selective laser melted thin-walled parts by response surface method, Opt. Lasers Eng. 103 (2018) 34-45.

http://dx.doi.org/10.1016/j.optlaseng.2017.11.011

[2] Morgan, R., C. J. Sutcliffe, W. O′ Neill, Density analysis of direct metal laser re-melted 316L stainless steel cubic primitives, J. Mater. Sci. 39.4 (2004) 1195-1205.

http://dx.doi.org/10.1023/B:JMSC.0000013875.62536.fa

[3] Herzog, Dirk, Vanessa Seyda, Eric Wycisk, Claus Emmelmann, Additive manufacturing of metals,

Acta Mater. 117 (2016) 371-92.

http://dx.doi.org/10.1016/j.actamat.2016.07.019

[4] Kunze, Karsten, Thomas Etter, Jürgen Grässlin, Valery Shklover, Texture, anisotropy in microstructure and mechanical properties of IN738LC Alloy processed by selective laser melting (SLM), Mater. Sci. Eng. A 620 (2015) 213-22.

http://dx.doi.org/10.1016/j.msea.2016.03.036

[5] Rickenbacher, L., T. Etter, S. Hövel, K. Wegener, High temperature material properties of NI738LC processed by selective laser melting (SLM) Technology, Rapid Prototyp. J. 19 No. 4 (2013) 282-90.

http://dx.doi.org/10.1108/13552541311323281

[6] Engeli, Roman, Thomas Etter, Simone Hövel, Konrad Wegener, Processability of different IN738LC powder batches by selective laser melting, J. Mater. Process. Technol. 229 (2016) 484-91.

http://dx.doi.org/10.1016/j.jmatprotec.2015.09.046

[7] Geiger, Fabian, Karsten Kunze, Thomas Etter, Tailoring the texture of IN738LC processed by selective laser melting (SLM) by specific scanning strategies, Mater. Sci. Eng. A 661 (2016) 240-46.

http://dx.doi.org/10.1016/j.msea.2016.03.036

[8] Guraya, T., S. Singamneni, Z. W. Chen, Microstructure formed during selective laser melting of IN738LC in keyhole mode, J. Alloys Compd. 792 (2019) 151-60.

http://dx.doi.org/10.1016/j.jallcom.2019.03.419

[9] Gu, Dongdong, Yves-Christian Hagedorn, Wilhelm Meiners, Konrad Wissenbach, Reinhart

Poprawe, Selective laser melting of in-Situ Tic/Ti$_5$Si$_3$ composites with novel reinforcement architecture and elevated performance, Surf. Coat. Technol. 205, No. 10 (2011) 3285-92.

http://dx.doi.org/10.1016/j.surfcoat.2010.11.051

[10] Li, X. P., G. Ji, Z. Chen, A. Addad, Y. Wu, H. W. Wang, J. Vleugels, J. Van Humbeeck, J. P. Kruth, Selective laser melting of nano-TiB$_2$ decorated AlSi10Mg alloy with high fracture strength and ductility, Acta Mater. 129 (2017) 183-93.

http://dx.doi.org/10.1016/j.actamat.2017.02.062

[11] Xia, Mujian, Dongdong Gu, Chenglong Ma, Hongyu Chen, Hongmei Zhang, Microstructure evolution, mechanical response and underlying thermodynamic mechanism of multi-phase strengthening WC/Inconel 718 composites using selective laser melting, J. Alloys Compd. 747 (2018) 684-95.

http://dx.doi.org/10.1016/j.jallcom.2018.03.049

[12] Martin, J. H., B. D. Yahata, J. M. Hundley, J. A. Mayer, T. A. Schaedler, T. M. Pollock, 3D printing of high-strength aluminium alloys, Nature 549, No. 7672 (Sep 20 2017) 365-69.

http://dx.doi.org/10.1038/nature23894

[13] Song, Bo, Shujuan Dong, Pierre Coddet, Genshu Zhou, Sheng Ouyang, Hanlin Liao, Christian Coddet, Microstructure and tensile behavior of hybrid nano-micro SiC reinforced iron matrix composites produced by selective laser melting, J. Alloys Compd. 579 (2013) 415-21.

http://dx.doi.org/10.1016/j.jallcom.2013.06.087

[14] Sun, Duanjun, Chunyuan Liang, Jinlong Shang, Jihui Yin, Yaru Song, Weizhou Li, Tianquan Liang, Xiuhai Zhang, Effect of Y$_2$O$_3$ contents on oxidation resistance at 1150 °C and mechanical properties at room temperature of ODS Ni-20Cr-5Al alloy, Appl. Surf. Sci. 385 (2016) 587-96.

http://dx.doi.org/10.1016/j.apsusc.2016.05.143

[15] Vasquez, Elodie, Pierre-François Giroux, Fernando Lomello, Aziz Chniouel, Hicham Maskrot, Frédéric Schuster, Philippe Castany, Elaboration of oxide dispersion strengthened fe-14cr stainless steel by selective laser melting, J. Mater. Process. Technol. 267 (2019) 403-13.

http://dx.doi.org/10.1016/j.jmatprotec.2018.12.034

[16] Li, Meiyan, Bin Han, Yong Wang, Kejin Pu, Effects of La_2O_3 on the microstructure and property of laser cladding Ni-based ceramic coating, Optik 130 (2017) 1032-37.

http://dx.doi.org/10.1016/j.ijleo.2016.11.111

[17] Chen, Y., Sridharan, K., Ukai, S., & Allen, T. R., Oxidation of 9Cr oxide dispersion strengthened steel exposed in supercritical water, J. Nucl. Mater. 371(1-3) (2007) 118-128.

http://dx.doi.org/10.1016/j.jnucmat.2007.05.018

[18] Balikci, E., Mirshams, R. A., & Raman, A., Fracture behavior of superalloy IN738LC with various precipitate microstructures, Mater. Sci. Eng. A 265(1-2) (1999) 50-62.

https://dx.doi.org/10.1016/S0921-5093(99)00012-X

[19] Arnold, K., Tatlock, G., Kenel, C., Colella, A., & Matteazzi, P., High temperature isothermal oxidation behaviour of an oxide dispersion strengthened derivative of IN625, Mater. High Temp. 35(1-3) (2017) 141-150. http://dx.doi.org/10.1080/09603409.2017.1393145

[20] Hong, C., Gu, D., Dai, D., Alkhayat, M., Urban, W. et al., Laser additive manufacturing of ultrafine TiC particle reinforced Inconel 625 based composite parts: Tailored microstructures and enhanced performance, Mater. Sci. Eng. A 635 (2015) 118-128.

https://doi.org/10.1016/j.msea.2015.03.043

[21] Gu, D., Wang, H., Dai, D., Yuan, P., Meiners, W., Poprawe, R., Rapid fabrication of Al-based bulk-

form nanocomposites with novel reinforcement and enhanced performance by selective laser melting, Scripta Mater. 96 (2015) 25-28. https://doi.org/10.1016/j.scriptamat.2014.10.011

[22] M.B. Wilms, R. Streubel, F. Fömel, A. Weisheit, J. Tenkamp, F. Walther, S. Barcikowski, J. H. Schleifenbaum, B. Gökce, Laser additive manufacturing of oxide dispersion strengthened steels using laser-generated nanoparticle-metal composite powders, Procedia CIRP 74 (2018) 196-200 https://doi.org/10.1016/j.procir.2018.08.093

[23] Zhou, Y., Lu, X., Xiang, H., Feng, Z., Preparation, mechanical, and thermal properties of a promising thermal barrier material: $Y_4Al_2O_9$, J. Adv. Ceram. 4(2) (2015) 94-102. https://doi.org/10.1007/s40145-015-0141-5

[24] Zhan, X., Li, Z., Liu, B., Wang, J., Zhou, Y., Hu, Z., Ching, W. Y., Theoretical Prediction of Elastic Stiffness and Minimum Lattice Thermal Conductivity of $Y_3Al_5O_{12}$, $YAlO_3$ and $Y_4Al_2O_9$, J. Am. Ceram. Soc. 95(4) (2012) 1429-1434.
https://doi.org/10.1111/j.1551-2916.2012.05118.x

[25] Quested, P. N., Brooks, R. F., Chapman, L., Morrell, R., Youssef, Y., Mills, K. C., Measurement and estimation of thermophysical properties of nickel based superalloys, Mater. Sci. Technol. 25(2) (2013) 154-162. https://doi.org/10.1179/174328408x361454

[26] Li, S., Chen, X., Zhou, Y., Song, G., Influence of grain size on high temperature oxidation behavior of Cr2AlC ceramics, Ceram. Int. 39(3) (2013) 2715-2721.
http://dx.doi.org/10.1016/j.ceramint.2012.09.039

[27] Trindade, V., Christ, H.-J., Krupp, U., Grain-Size Effects on the High-Temperature Oxidation Behaviour of Chromium Steels, Oxid. Met. 73(5-6) (2010) 551-563.
http://dx.doi.org/10.1007/s11085-010-9192-8

[28] Jo, T. S., Kim, S. H., Kim, D.-G., Park, J. Y., Kim, Y. D., Effects of grain refinement on internal oxidation of Alloy 617, J. Nucl. Mater. 402(2-3) (2010) 162-166.

https://doi.org/10.1016/j.jnucmat.2010.05.013

[29] Perez, P., Influence of the alloy grain size on the oxidation behaviour of PM2000 alloy, Corros. Sci. 44(8) (2002) 1793-1808.

https://doi.org/10.1016/S0010-938X(01)00182-2

[30] Kim, J. H., Kim, K. M., Byun, T. S., Lee, D. W., Park, C. H., High-temperature oxidation behavior of nano-structured ferritic oxide dispersion-strengthened alloys, Thermochim. Acta 579 (2014) 1-8.

https://doi.org/10.1016/j.tca.2014.01.010

[31] Zheng, H. Z., Lu, S. Q., Huang, Y., Influence of grain size on the oxidation behavior of NbCr2 alloys at 950–1200°C, Corros. Sci. 51(2) (2009) 434-438.

https://doi.org/10.1016/j.corsci.2008.11.014

[32] Wang, Yan, Yong Liu, Hui-ping Tang, Weijie Li, Chao Han, Oxidation behavior and mechanism of porous nickel-based alloy between 850 and 1000 °C, Trans. Nonferrous Met. Soc. China 27, No. 7 (2017) 1558-68.

http://dx.doi.org/10.1016/s1003-6326(17)60177-8

[33] T. Zhou, T.C. Yuan, Z.Y. Li, K.C. Zhou, Comparison of oxidation-resistance property between two kinds of Ni-Fe alloys, Min. Metall. Eng. 26 (2006) 68–71.

http://dx.doi.org/10.1007/s11434-006-2076-2

[34] Su, Yuling, Jinjin Guo, Xuerui Cheng, Shiquan Feng, Yang Yang, Intrinsic anharmonicity effect in $YCrO_3$: pressure and temperature dependent Raman spectra studies, J. Alloys Compd. 805

(2019) 489-95.

http://dx.doi.org/10.1016/j.jallcom.2019.07.087

[35] Kim, Jeoung Han, Kyong Min Kim, Thak Sang Byun, Dong Won Lee, Chan Hee Park, High-temperature oxidation behavior of nano-structured ferritic oxide dispersion-strengthened alloys, Thermochim. Acta 579 (2014) 1-8.

http://dx.doi.org/10.1016/j.tca.2014.01.010

[36] Peruzzo, M., T. D. Beux, M. F. C. Ordoñez, R. M. Souza, M. C. M. Farias, High-temperature oxidation of sintered austenitic stainless steel containing boron or yttria, Corros. Sci. 129 (2017) 26-37.

http://dx.doi.org/10.1016/j.corsci.2017.09.002

[37] Stringer, J., B. A. Wilcox, R. I. Jaffee, The high-temperature oxidation of nickel-20 wt.wt% chromium alloys containing dispersed oxide phases, Oxid. Met. 5.1(1972) 11-47.

http://dx.doi.org/10.1007/BF00614617

[38] Bautista, A., F. Velasco, J. Abenojar, Oxidation resistance of sintered stainless steels: effect of yttria additions, Corros. Sci. 45, No. 6 (2003) 1343-54.

http://dx.doi.org/10.1016/s0010-938x(02)00217-2

[39] Wang, E., Sun, D., Liu, H., Lu, M., Guo, W., Zheng, B., Zhang, X., The Oxidation Behavior of Ni–15Cr–5Al–xSi (x = 0, 1, 3, 5 wt%) Alloys in Air at 1100 °C, Oxid. Met. 92 (2019), 3-4.

https://dx.doi.org/10.1007/s11085-019-09922-0

[40] Giggins, C. S., F. S. Pettit, Oxidation of NiCrAl Alloys Between 1000° and 1200°C, J. Electrochem. Soc. 118.11 (1971).

https://dx.doi.org/10.1149/1.2407837

[41] Lou, H., Wang, F., Zhu, S., Xia, B., Zhang, L., Oxide formation of K38G superalloy and its sputtered micrograined coating, Surf. Coat. Technol. 63(1-2) (1994) 105-114.

https://dx.doi.org/10.1016/S0257-8972(05)80014-3

[42] Zhao, W., Gleeson, B., Assessment of the detrimental effects of steam on Al_2O_3-scale establishment, Oxid. Met. 83(5-6) (2015) 607-627.

http://dx.doi.org/10.1007/s11085-015-9541-8

[43] Leblond, J. B., Pignol, M., Huin, D., Predicting the transition from internal to external oxidation of alloys using an extended wagner model, Comptes Rendus Mécanique, 341(3) (2013) 314-322.

https://dx.doi.org/10.1016/j.crme.2013.01.003

[44] Chou, Kuo-Chih, Qun Luo, Qian Li, Jie-Yu Zhang, Influence of the density of oxide on oxidation kinetics, Intermetallics 47 (2014) 17-22.

http://dx.doi.org/10.1016/j.intermet.2013.11.024

[45] Evans, H. E., R. C. Lobb, Conditions for the initiation of oxide-scale cracking and spallation, Corros. Sci. 24.3 (1984) 0-222.

http://dx.doi.org/10.1016/0010-938x(84)90051-9

[46] Stott, F. H., G. C. Wood, J. Stringer, The influence of alloying elements on the development and maintenance of protective scales, Oxid. Met. 44.1-2 (1995) 113-145.

http://dx.doi.org/10.1007/BF01046725

[47] N.B. Pilling, R.E. Bedworth, The oxidation of metals at high temperatures, J. Inst. Met. 29 (1923) 529

http://refhub.elsevier.com/S0010-938X(19)32102-X/sbref0060

[48] Mat Web, Material property data. http://www.matweb.com/index.aspx

[49] A.M. Huntz, Stresses in NiO, Cr_2O_3 and Al_2O_3 oxide scales, Mater. Sci. Eng. A, 201(1-2) (1995) 211-228.

https://dx.doi.org/10.1016/0921-5093(94)09747-x

[50] H.E. Evans, Stress effects in high temperature oxidation of metals, Int. Mater. Rev. 40 (1995) 1–40.

https://dx.doi.org/10.1179/imr.1995.40.1.1

[51] Barnes, J. J., Goedjen, J. G., Shores, D. A., A Model for stress generation and relief in oxide—Metal systems during a temperature change, Oxid. Met. 32(5-6) (1989) 449-469.

https://dx.doi.org/10.1007/bf00665449

[52] Li, N., Xiao, J., Prud'homme, N., Chen, Z., Ji, V., Residual stresses in oxide scale formed on fe-17cr stainless steel, Appl. Surf. Sci. 316 (2014) 108-113.

https://dx.doi.org/10.1016/j.apsusc.2014.07.195

[53] Quested, P. N., R. F. Brooks, L. Chapman, R. Morrell, Y. Youssef, K. C. Mills, Measurement and estimation of thermophysical properties of nickel-based superalloys, Mater. Sci. Technol. 25(2) (2013) 154-162.

https://doi.org/10.1179/174328408X361454

[54] Hou, P. Y., Stringer, J., The effect of reactive element additions on the selective oxidation, growth and adhesion of chromia scales, Mater. Sci. Eng. A 202(1-2) (1995) 1-10.

https://dx.doi.org/10.1016/0921-5093(95)09798-8

[55] Stringer, J., The reactive element effect in high-temperature corrosion, Mater. Sci. Eng. A 120-121(part-P1) (1989) 129-137.

https://dx.doi.org/10.1016/0921-5093(89)90730-

[56] Seal, S., Kuiry, S. C., Bracho, L. A., Surface chemistry of oxide scale on in-738lc superalloy: effect of long-term exposure in air at 1173 k, Oxid. Met. 57(3-4) (2002) 297-322.

https://dx.doi.org/10.1023/a:1014878402960

Figure Captions
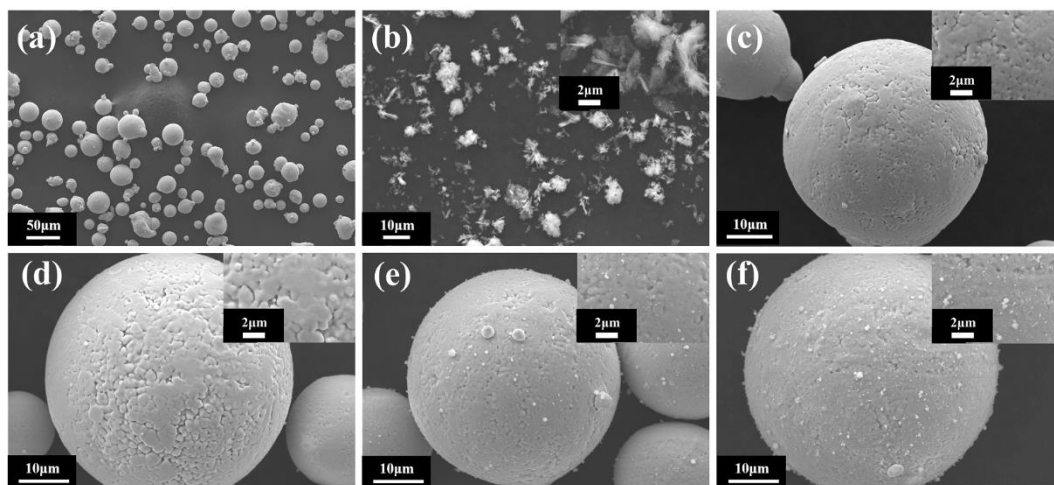
Fig. 1. SEM images of the powder morphologies, (a) IN738LC, (b) Y_2O_3, the mixture powders with (c) 0 wt% Y_2O_3, (d) 0.05 wt% Y_2O_3, (e) 0.2 wt% Y_2O_3, (f) 0.6 wt% Y_2O_3, the insert images showing the details of the powder surfaces in high magnification.
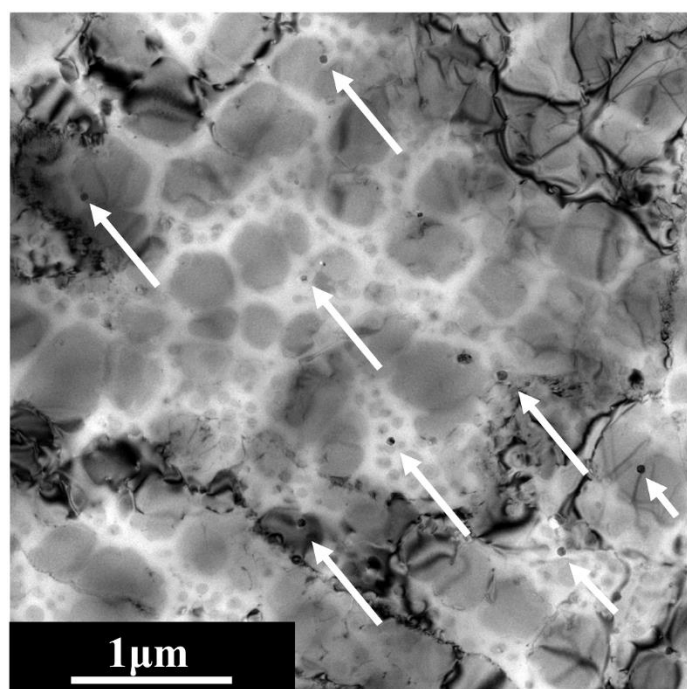
Fig. 2. TEM image of the alloy containing 0.05 wt% Y_2O_3 showing the distribution of the added nano-sized particles (white arrow).
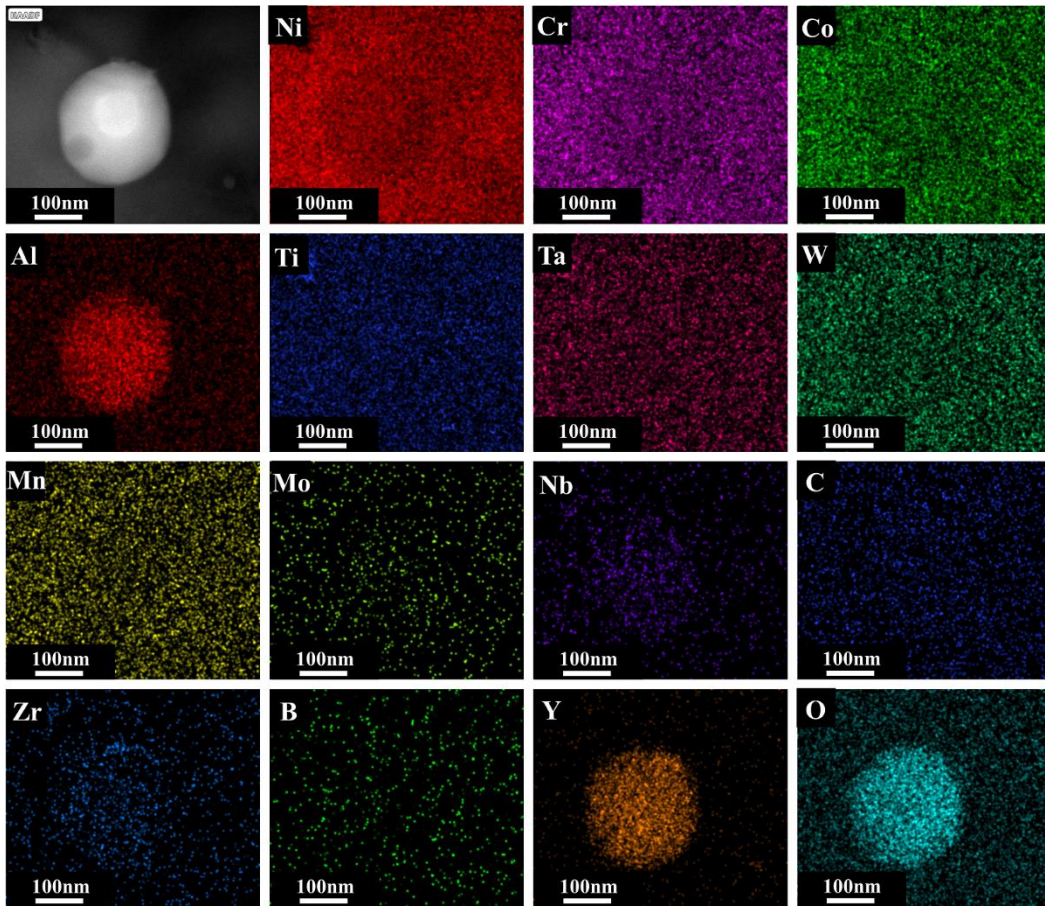
Fig. 3. STEM EDS mapping results of the nano-sized particle.
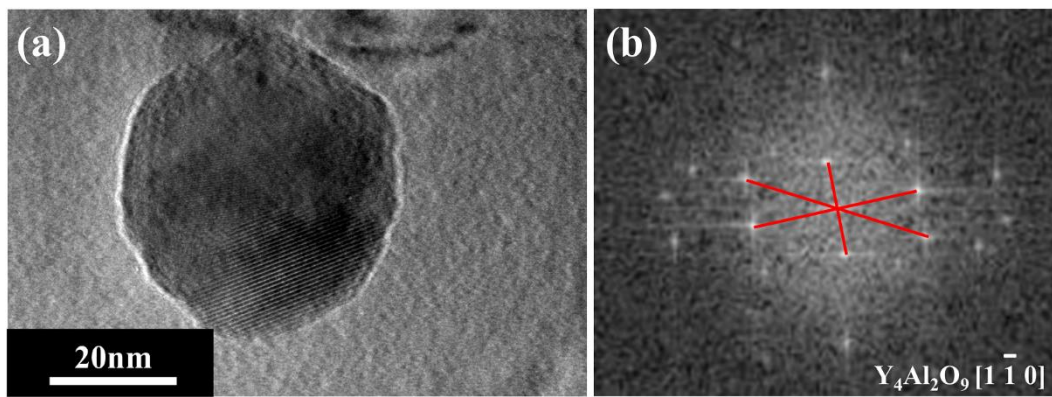
Fig. 4. (a) TEM image of the added nano-sized particle in high magnification, (b) the corresponding

Fast Fourier Transformation (FFT) image of the nano-sized particle.
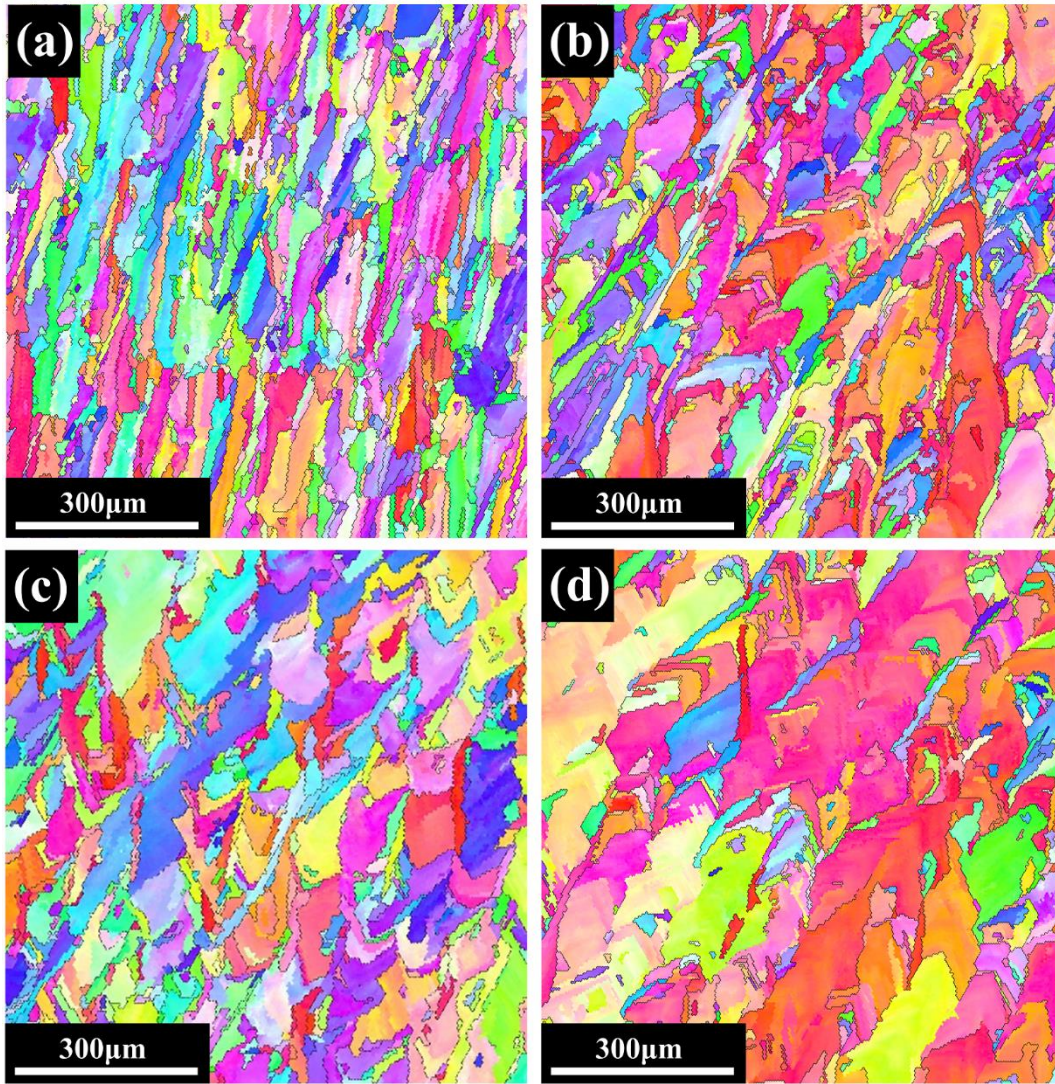
Fig. 5. EBSD maps showing the IPFs of (a) the alloy without Y_2O_3 and the alloys containing (b) 0.05 wt%, (c) 0.2 wt% and (d) 0.6 wt% Y_2O_3 before the oxidation tests.
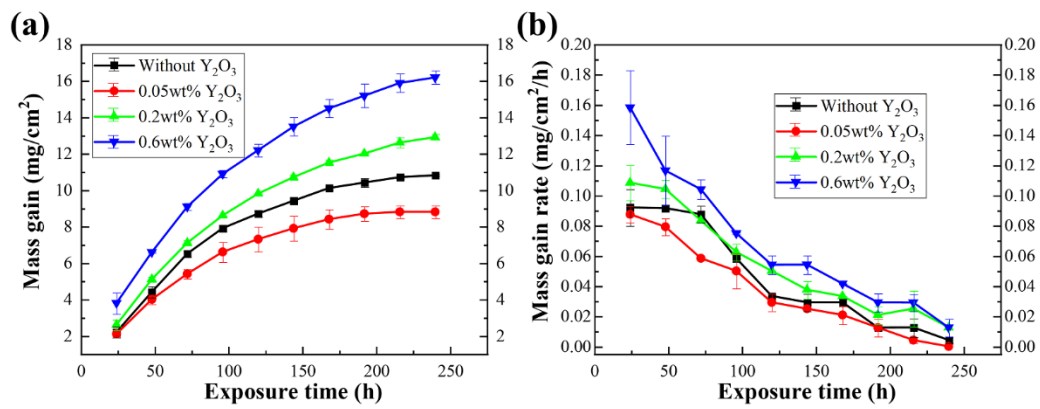
Fig. 6. (a) Mass gain and (b) mass gain rate as a function of the exposure time.
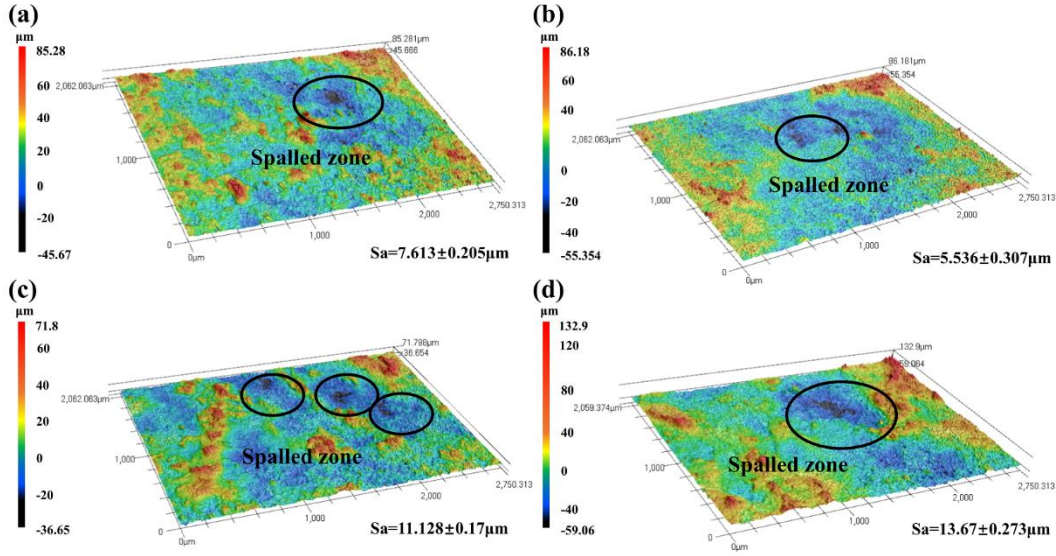
Fig. 7. 3D reconstruction images of the oxide scale surfaces after the oxidation tests at 1095 ºC for 240 h of (a) the alloy without Y_2O_3 and the alloys containing (b) 0.05 wt%, (c) 0.2 wt% and (d) 0.6 wt% Y_2O_3 by LSCM and the corresponding surface roughness.
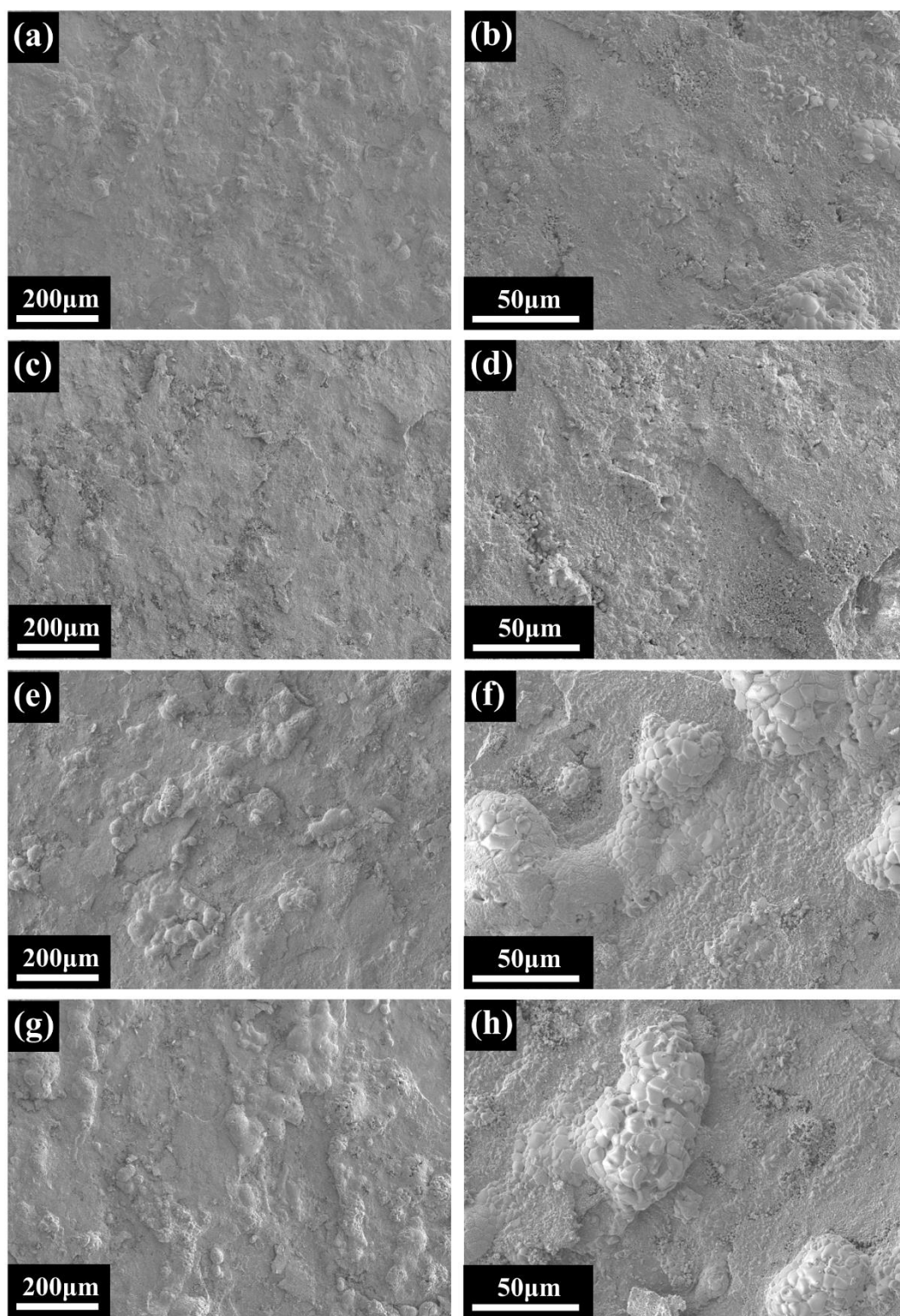
Fig. 8. SEM images of the oxide scale surfaces after the oxidation tests at 1095 °C for 240 h of (a,b) the alloy without Y_2O_3 and the alloys containing (c,d) 0.05 wt%, (e,f) 0.2 wt% and (g,h) 0.6 wt% Y_2O_3 in low and high magnifications.
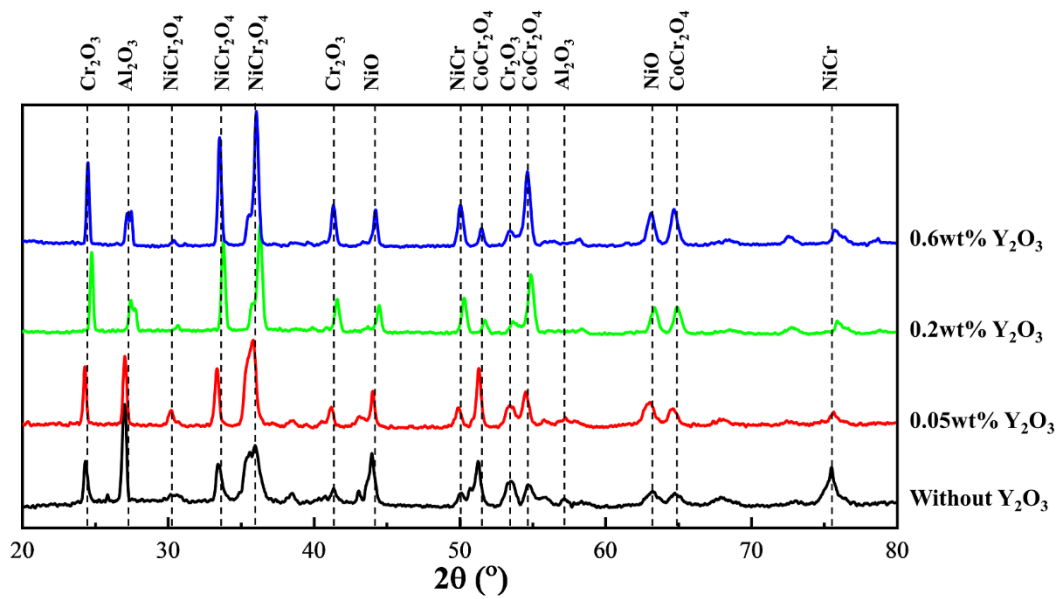
Fig. 9. XRD patterns of the oxide scale surfaces after the oxidation tests at 1095 °C for 240 h of the alloys with different contents of the Y_2O_3 nanoparticles.
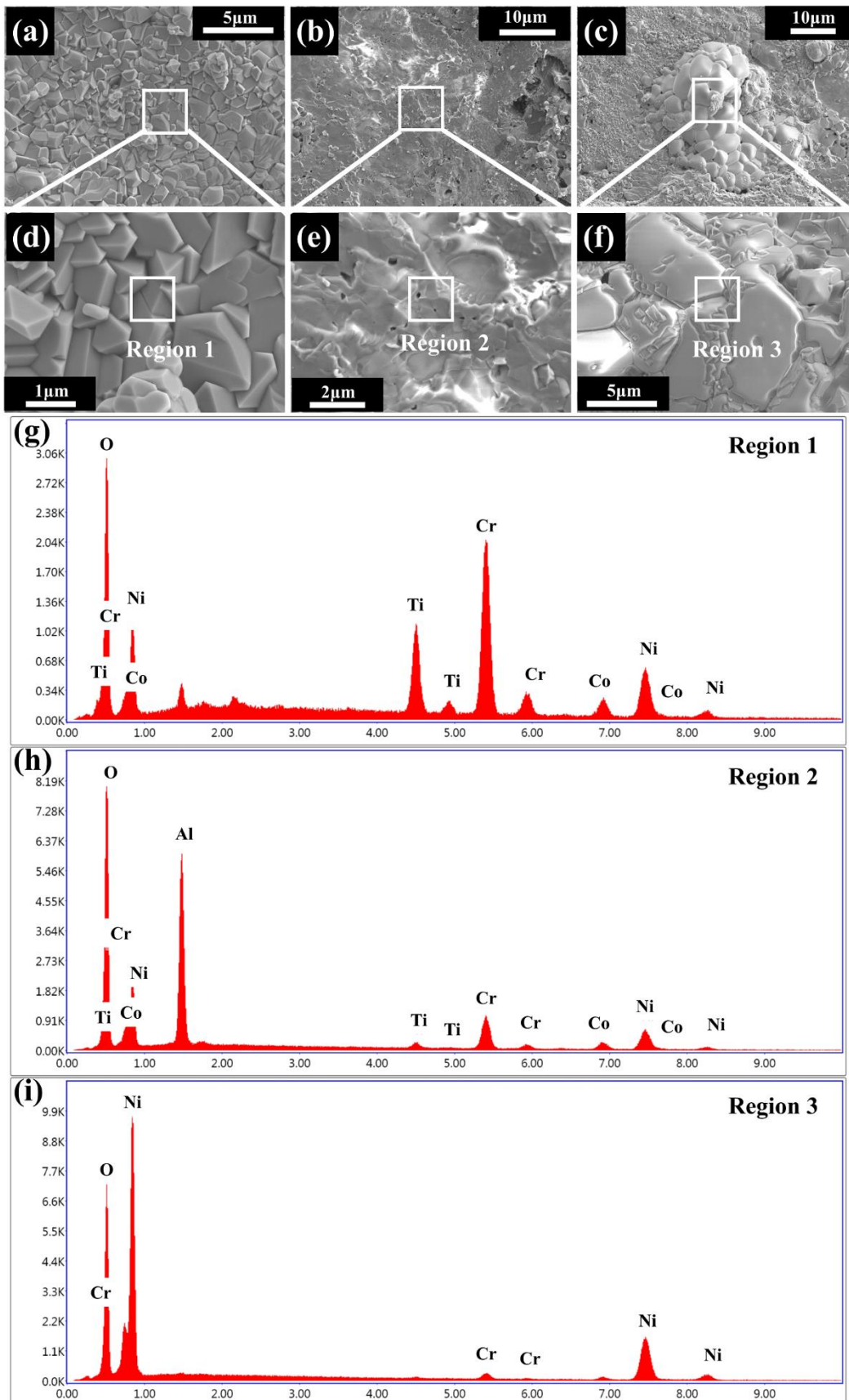
Fig. 10. SEM images of the oxide scale surface after the oxidation tests at 1095 °C for 240 h of the

alloy without Y_2O_3, indicating three different morphologies, i.e., (a,d) crystalline, (b,e) lamellar and (c,f) nodular, (g), (h) and (i) showing the EDS analysis on the corresponding morphological regions.
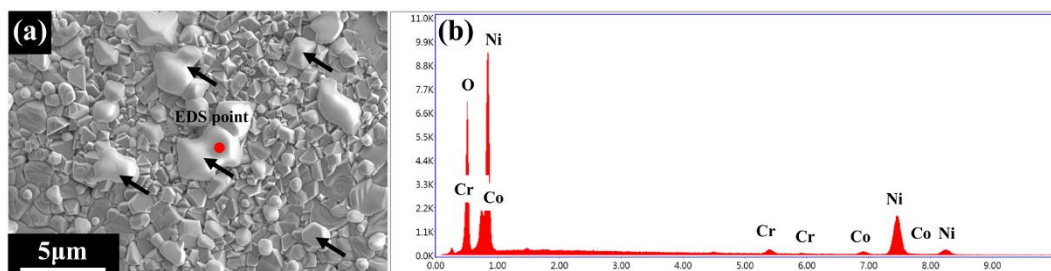
Fig. 11. (a) SEM image of the nodular structures after the oxidation tests at 1095 ℃ for 240 h of the alloy containing 0.05 wt% Y_2O_3 and (b) the corresponding EDS result.
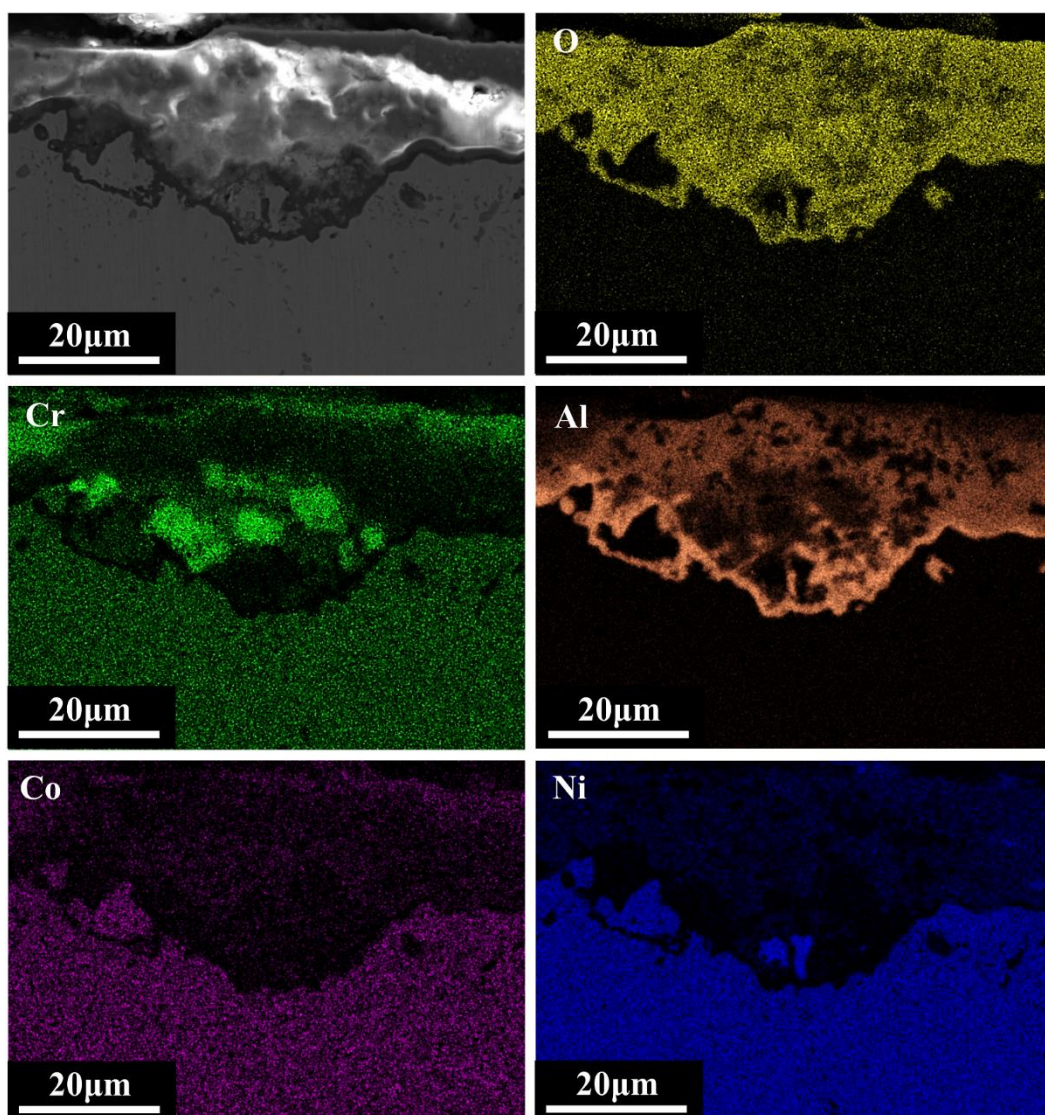
Fig. 12. EDS chemical composition mapping of the oxide scale after the oxidation tests at 1095 ℃ for

240 h of the alloy without Y$_2$O$_3$.
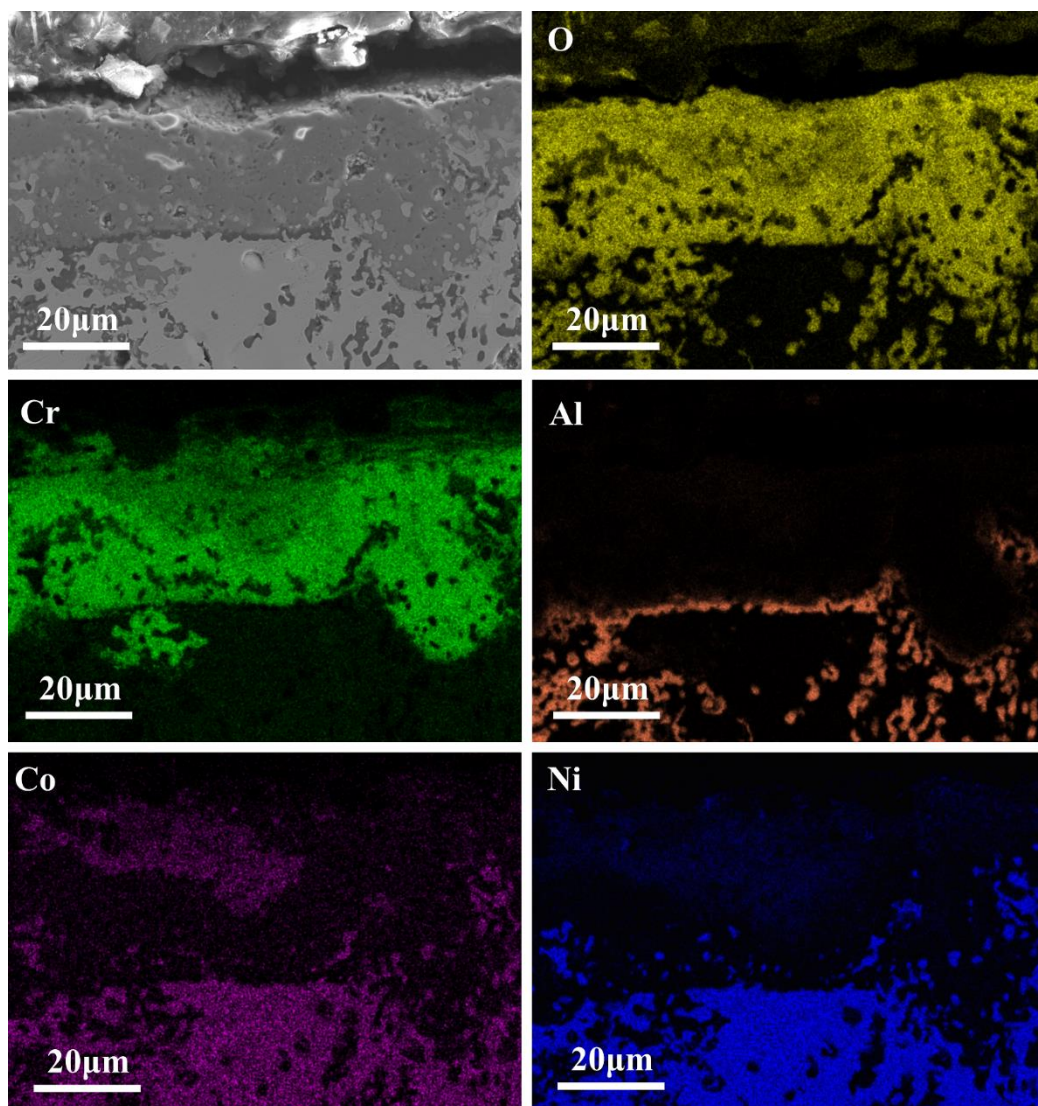
Fig. 13. EDS chemical composition mapping of the oxide scale after the oxidation tests at 1095 ºC for 240 h of the alloy containing 0.6 wt% Y$_2$O$_3$.
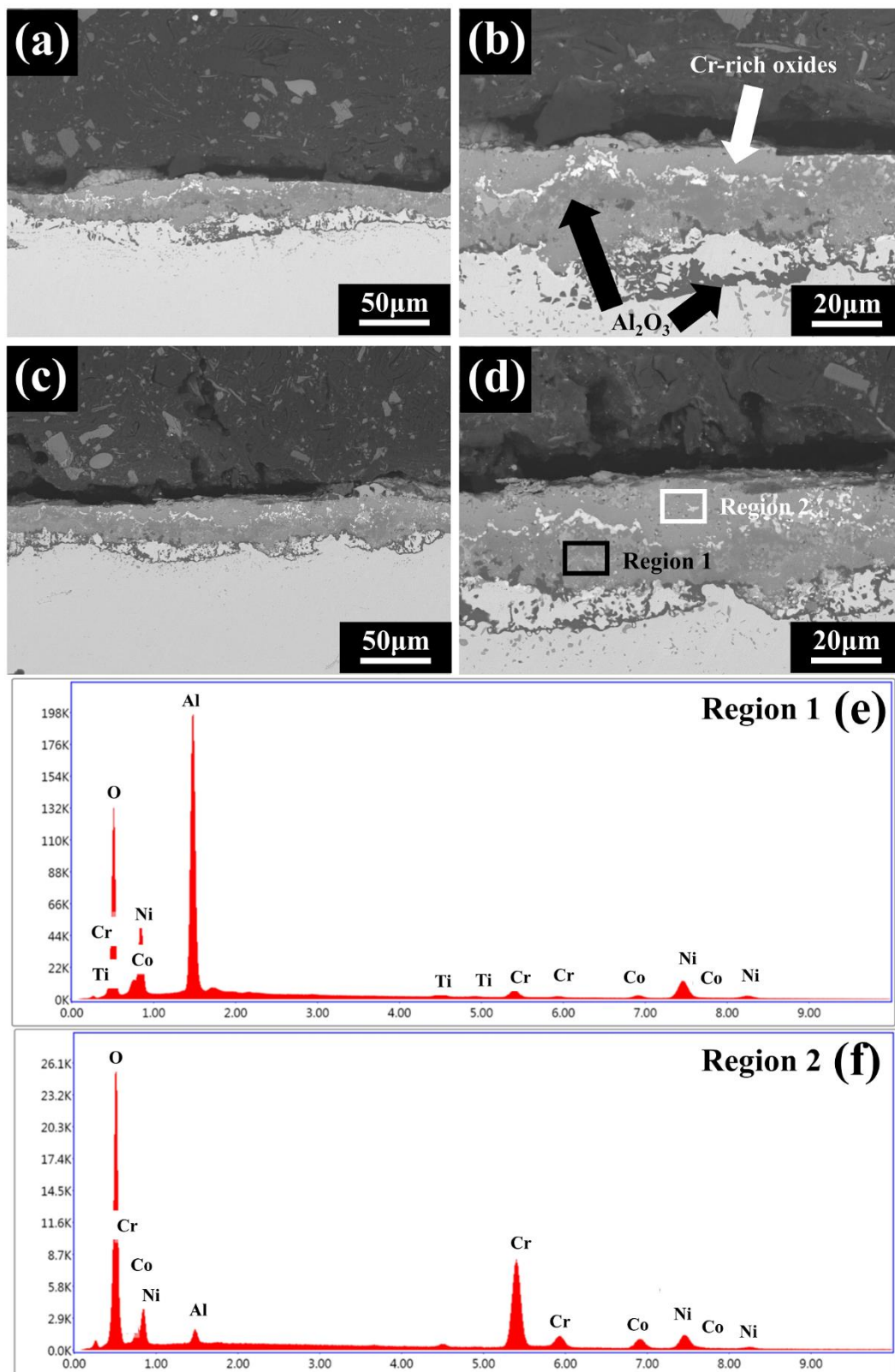
Fig. 14. SEM images of the oxide scales after the oxidation tests at 1095 °C for 240 h of (a,b) the alloy without Y_2O_3 and the alloy containing (c,d) 0.05 wt% Y_2O_3 in low and high magnifications, (e) EDS result of Region 1 and (f) EDS result of Region 2.
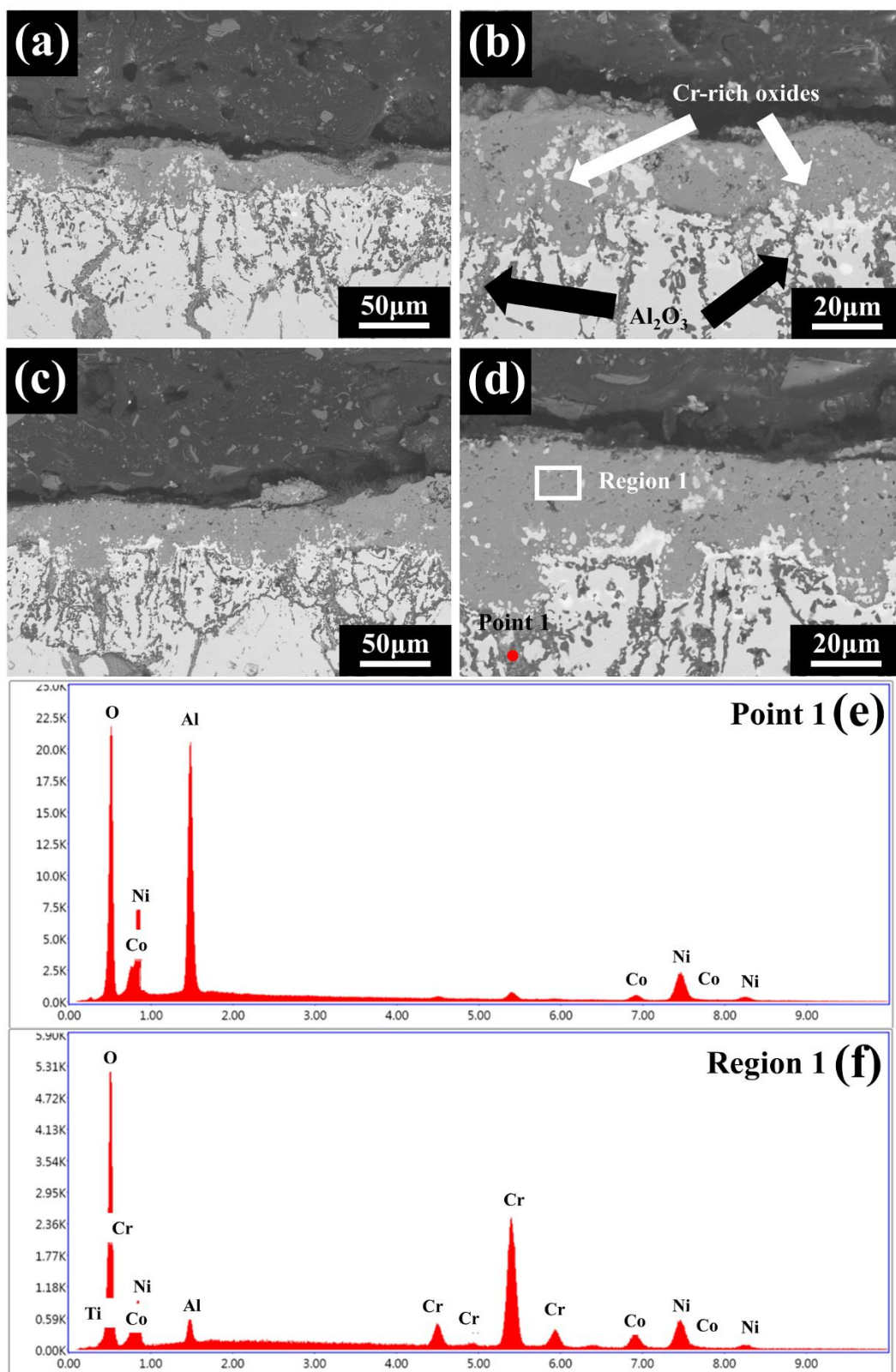
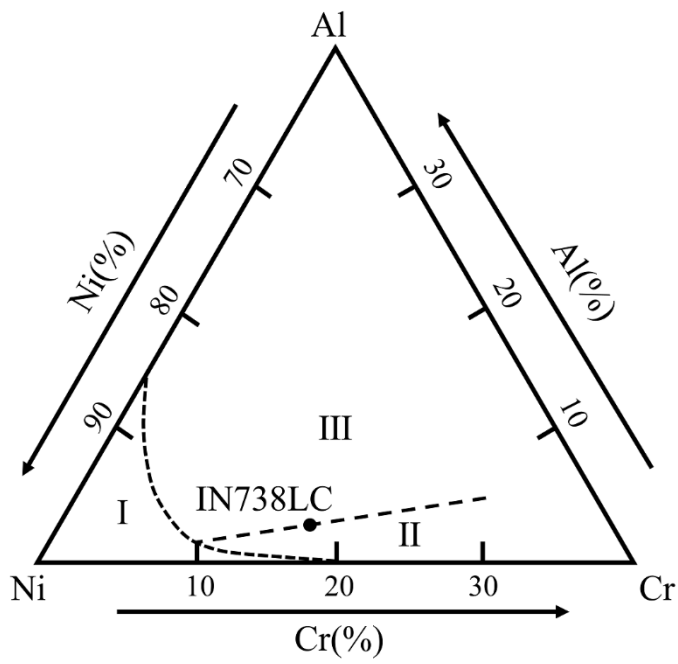Fig. 15. SEM images of the oxide scales after the oxidation tests at 1095 $^{\circ}$C for 240 h of the alloys containing (a,b) 0.2 wt% and (c,d) 0.6 wt% Y_2O_3 in low and high magnifications, (e) EDS result of Point 1 and (f) EDS result of Region 1.

Fig. 16. The isothermal diagram [40] showing the compositional limits for these three mechanisms of oxidation in the Ni-Cr-Al system.
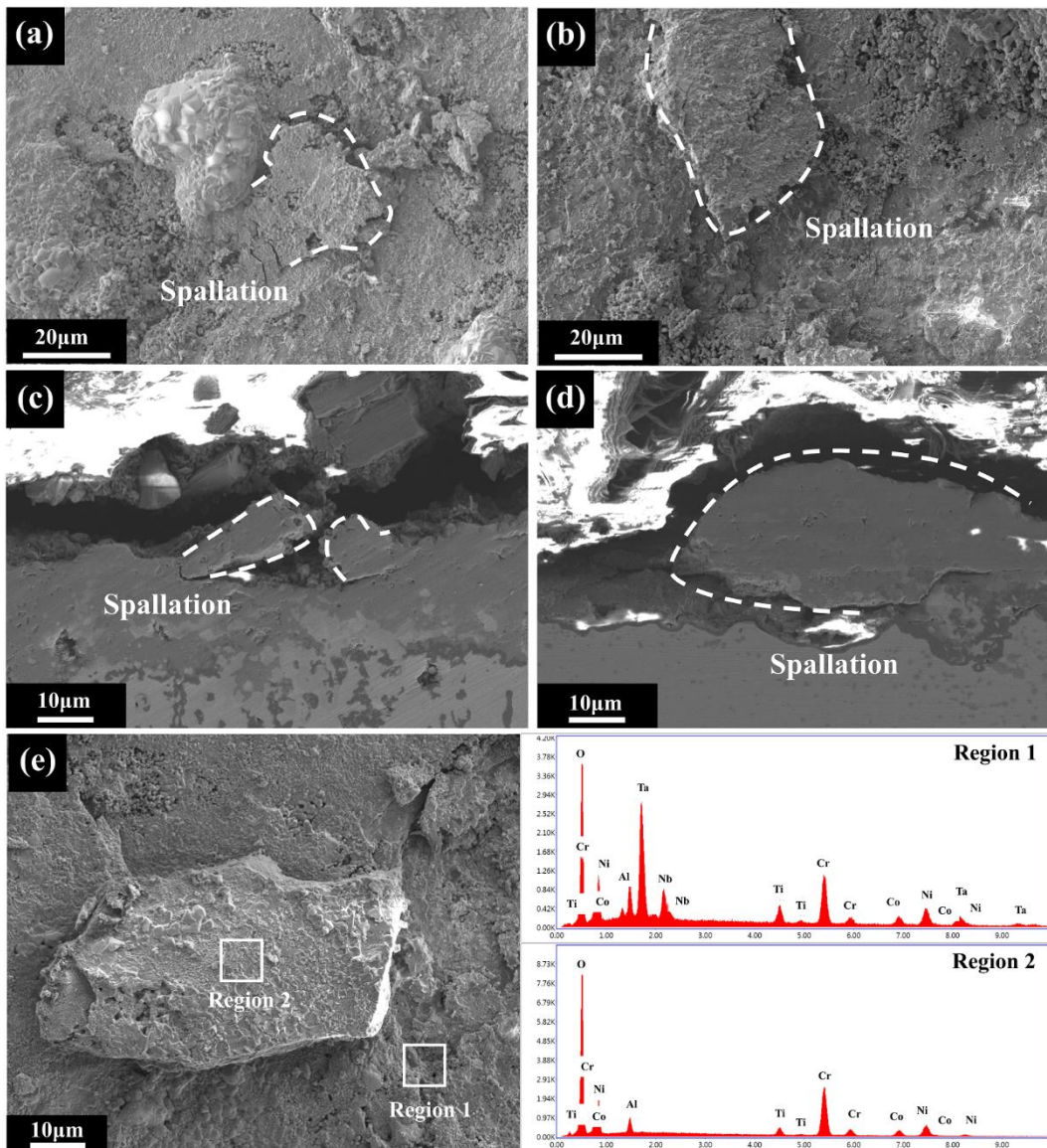
Fig. 17. SEM images of the spallation phenomenon after the oxidation tests at 1095 °C for 240 h observed from the oxide scale surfaces of the alloys containing (a) 0.2 wt% and (b) 0.6 wt% Y_2O_3 and from the oxide scale cross-sections of the alloys containing (c) 0.2 wt% and (d) 0.6 wt% Y_2O_3. (e) an example of the oxide scale spallation and the corresponding EDS results.
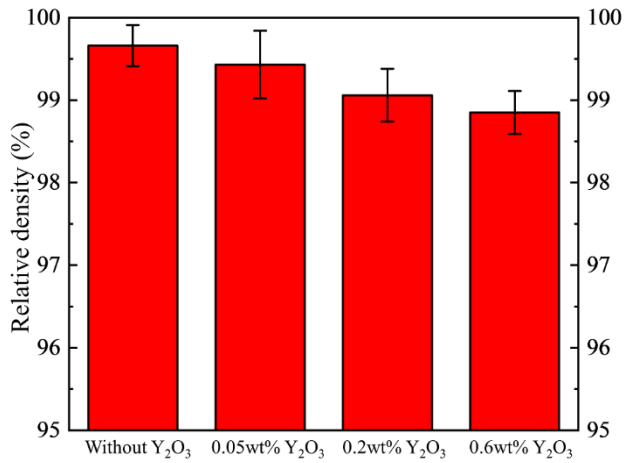
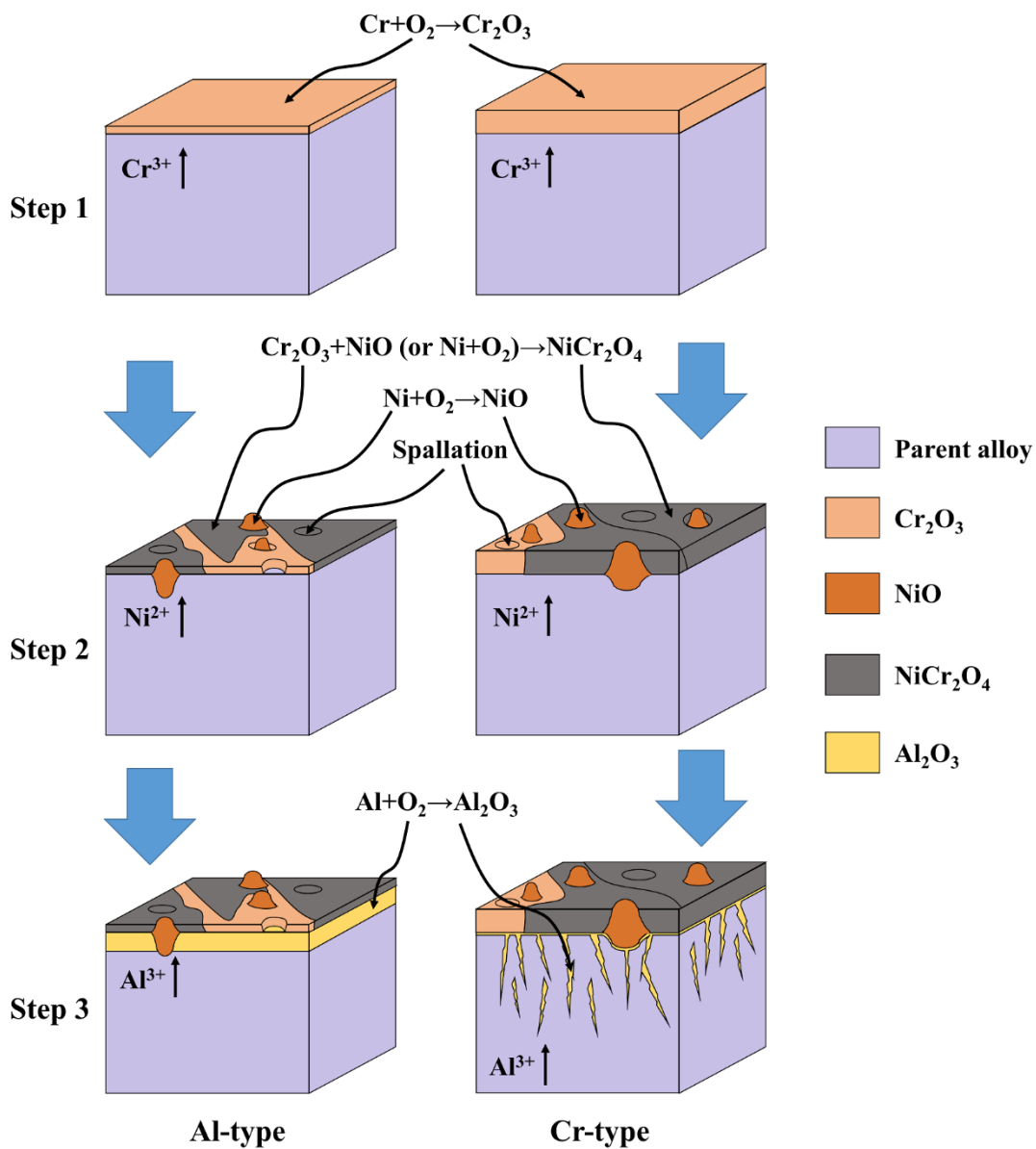Fig. 18. Relative density as a function of the Y_2O_3 content.

Fig. 19. A schematic diagram showing the oxidation mechanism of the LPBF-processed IN738LC components

at 1095 ºC with the oxide scale in Al-type and Cr-type.